Volume 59
Number 11
7 February 2023
Pages 1385–1542

ChemComm

Chemical Communications

rsc.li/chemcomm

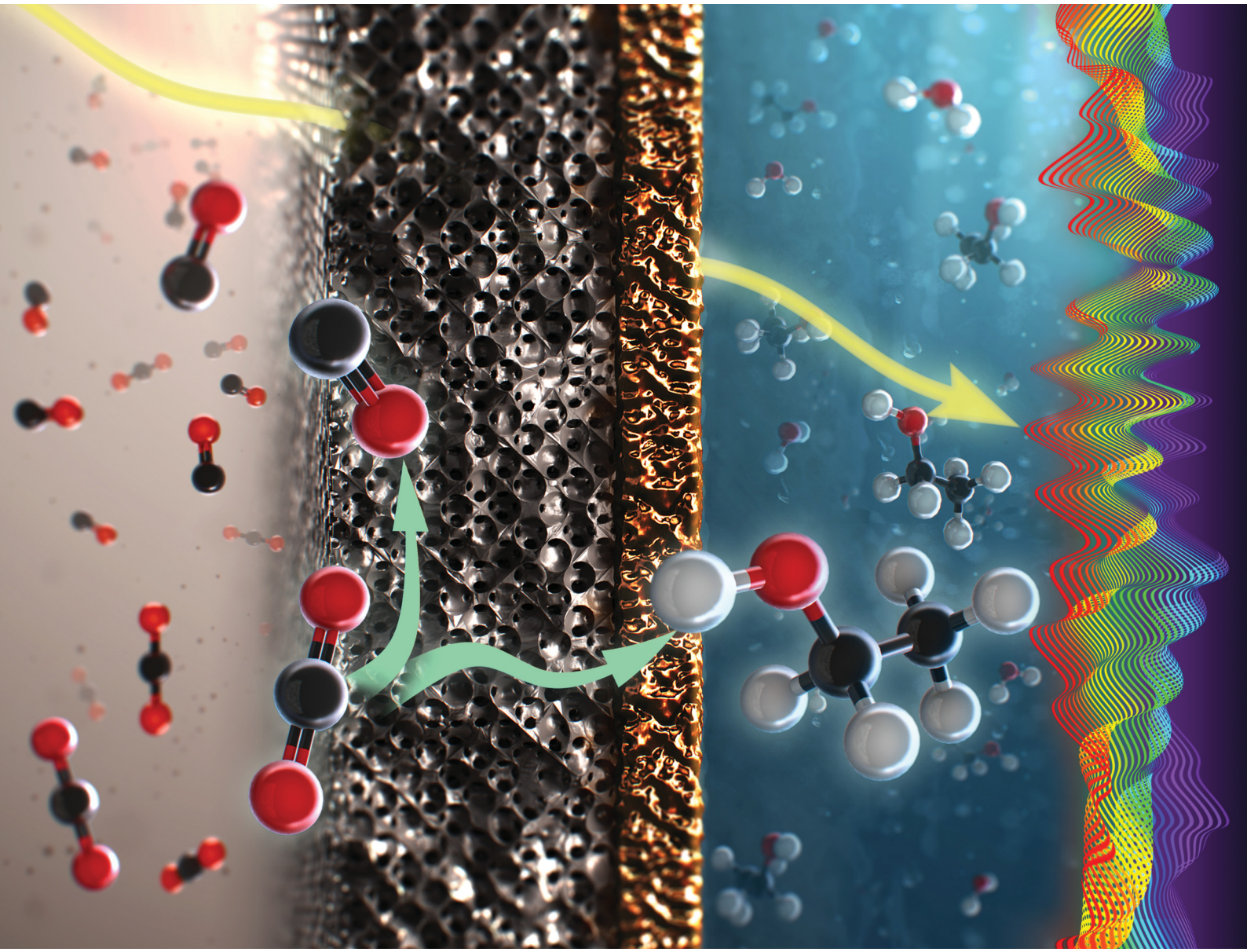

ISSN 1359-7345

ROYAL SOCIETY OF CHEMISTRY

FEATURE ARTICLE

Dorottya Hursán and Csaba Janáky

Operando characterization of continuous flow CO_2 electrolyzers: current status and future prospects

ChemComm

FEATURE ARTICLE

View Article Online
View Journal | View Issue

Cite this: *Chem. Commun.*, 2023, **59**, 1395

Operando characterization of continuous flow CO_2 electrolyzers: current status and future prospects

Dorottya Hursán and Csaba Janáky *

Received 9th November 2022,
Accepted 3rd January 2023

DOI: 10.1039/d2cc06065e

rsc.li/chemcomm

The performance of continuous-flow CO_2 electrolyzers has substantially increased in recent years, achieving current density and selectivity (particularly for CO production) meeting the industrial targets. Further improvement is, however, necessary in terms of stability and energy efficiency, as well as in high-value multicarbon product formation. Accelerating this process requires deeper understanding of the complex interplay of chemical–physical processes taking place in CO_2 electrolyzer cells. *Operando* characterization can provide these insights under working conditions, helping to identify the reasons for performance losses. Despite this fact, only relatively few studies have taken advantage of such methods up to now, applying *operando* techniques to characterize practically relevant CO_2 electrolyzers. These studies include X-ray absorption- and Raman spectroscopy, fluorescent microscopy, scanning probe techniques, mass spectrometry, and radiography. Their objective was to characterize the catalyst structure, its microenviroment, membrane properties, *etc.*, and relate them to the device performance (reaction rates and product distribution). Here we review the current state-of-the-art of *operando* methods, associated challenges, and also their future potential. We aim to motivate researchers to perform *operando* characterization in continuous-flow CO_2 electrolyzers, to understand the reaction mechanism and device operation under practically relevant conditions, thereby advancing the field towards industrialization.

Introduction

Electrochemical CO_2 reduction (CO_2RR) is a rising technology to produce fuels and commodity chemicals in a possibly carbon neutral- or even negative way.[1] Being an electrochemical process, it can be directly coupled to renewable electricity (*e.g.*, solar, wind), assisting the storage of these intermittent energy sources in the form of chemical bonds,[2] while reducing the dependence of our society on fossil fuel resources at the same time. Systematic investigation of CO_2RR started in the 1990s when the main focus was on the exploration of selectivity trends for different metal electrodes.[3] Over the years, materials engineering strategies, such as nanostructuring,[4] alloying[5,6] or novel materials design (*e.g.*, non-metal electrodes),[7,8] were explored to increase activity or to steer selectivity towards the formation of a given product. Additionally, the modification of the catalyst microenvironment, by electrode and electrolyte design, also turned out to be critically important to improve catalyst performance.[9] In parallel, detailed mechanistic investigation of the CO_2RR[10] was also performed, which largely contributed to our current understanding of the reaction paths leading to certain products. *In situ* and *operando* spectroscopic investigations have become the most powerful tools for gaining mechanistic understanding,[11] as only these methods are capable of tracking changes in the catalyst structure, its microenvironment, and reaction intermediates during operation. The improvement of spectroscopic techniques in terms of signal intensity (also in electrolytes), and spatial and temporal resolution has opened up new possibilities for *operando* characterization, and these techniques are rather commonly used in electrocatalysis research nowadays. Beyond online product detection methods, these include vibrational spectroscopy, X-ray based methods, local pH measurements and electron microscopy among others, thoroughly reviewed recently.[10,12–15]

In the past 10–15 years, with the emergence of continuous-flow electrolyzer cells, the field has started to expand towards practical applications.[16] As it became clear that the CO_2RR has relevance for industrialization, electrolyzer development had also become a focus of research. Researchers concentrating on catalyst development tend to benchmark their catalysts in flow electrolyzers too[17,18] to demonstrate the potential for practical application, already at the early stage of catalyst development. Several cell designs exist for low temperature CO_2 electrolysis,[16] which differ in the presence/absence of electrolytes and ion transport characteristics among others. Each of these cells has

University of Szeged, Department of Physical Chemistry and Materials Science, Aradi sq. 1, Szeged, 6720, Hungary. E-mail: janaky@chem.u-szeged.hu

its specific advantages and limitations, but one feature is common: gas-phase CO_2 is introduced to the cathode gas diffusion electrode (GDE), instead of being dissolved in the electrolyte as in the "traditional" H-type cells.[19] The so-called triple-phase boundary, the gas/liquid/solid interface, results in improved mass transport for reactants and products. This leads to notably higher achievable CO_2RR product partial current densities (exceeding 1 A cm^{-2}),[20,21] but also poses different challenges during system operation. For instance, carbonate precipitation and crossover is a major hurdle in the long-term and efficient operation of anion-exchange membrane (AEM)-containing CO_2 electrolyzers.[22,23] Furthermore, the different microenvironments in flow *vs.* batch electrolyzers,[24] such as local pH and reactant/adsorbate concentrations, can open up new reaction pathways; therefore the mechanistic findings obtained in batch cells cannot explicitly be translated to flow conditions.

Despite the increasing number of flow cell studies to improve CO_2RR performance, and *operando* investigations in batch-type cells dedicated to mechanistic understanding, only relatively few studies (less than 40) exist on the combination of the two. The main reason probably lies in the technical and practical challenges associated with the implementation of *operando* characterization in full electrolyzer devices (because of their complex and relatively fixed geometry). This would be, however, indeed necessary, as the interplay of several processes (*e.g.*, cathode and anode reaction kinetics, ion transport, membrane properties) together determines the overall performance of these devices. *Operando* characterization of fuel cell and water electrolyzer devices is already at a more advanced stage.[25,26] Considering their similarity to CO_2 electrolyzers, these works can serve as examples and inspiration for the CO_2RR community.

Previous works on CO_2 electrolyzers have already nicely demonstrated the potential of *operando* methods towards the more realistic evaluation of catalyst/electrolyzer performance. Here, we review these studies with the aim to highlight how *operando* characterization can help to overcome the main challenges associated with CO_2 (and also CO) reduction. We note that although high-temperature CO_2 electrolyzers (*i.e.*, solid oxide electrolyzers) offer high conversion efficiencies, because of the favorable thermodynamics, and fast reaction kinetics at elevated temperatures, they are out of the scope of this review, as they are very different from low temperature electrolyzers, which are our main focus here.

Continuous-flow CO_2 reduction and status of the field

The main cell architectures for continuous-flow CO_2 electrolysis have been thoroughly reviewed elsewhere; therefore here we give only a brief description of the different designs.[16,23,27] The core component of continuous-flow CO_2 electrolyzers is the gas diffusion electrode (GDE),[28] allowing gas-phase CO_2 to reach the catalyst, which results in enhanced mass transport. Here we note that we use the "flow cell" as a general denomination for all the CO_2 electrolyzer devices employing gas-diffusion electrodes (GDE) with flowing gas-phase CO_2 as the reactant, including both the zero-gap and the microfluidic architectures. The catalyst layer is deposited on one side of the gas diffusion layer facing the catholyte (if present) and the ion-exchange membrane (IEM). This latter separates the cathode and anode compartments. In a zero-gap configuration, the anode and cathode catalysts are in direct contact with the membrane separator, which together are called the membrane electrode assembly (MEA). The surface chemistry of the catalysts is largely determined by the membrane in such cells, and can be significantly different from the case when the catalysts are in contact with a bulk electrolyte (H-type cells or flow cells with electrolyte layers).[29,30] The type of the separator determines the direction of the ion transport, which can be a cation-exchange (CEM), an anion-exchange (AEM), or a bipolar membrane (BPM; *i.e.*, a CEM and an AEM stacked together). Importantly, none of these membranes is perfectly permselective,[31] and even an AEM can let cations through (although in minor amounts), which turned out to be important in achieving high-performance AEM CO_2 electrolysis.[22]

The other major type of cell is the microfluidic device, employing a flowing electrolyte between the anode and cathode catalysts. In this configuration, it is possible that only one common electrolyte flows between the two electrodes,[32] but membrane-separated (hybrid) cells, with separate anolyte and catholyte channels, are more commonly used for research purposes.[33] In microfluidic electrolyzers a reference electrode can be placed in the catholyte and/or anolyte compartments, enabling the measurement of individual electrode potentials. This allows for easier decoupling of the processes happening in the cell. The microfluidic reactors are the most similar designs to the H-type cells, and thus are frequently used for catalyst testing at practically relevant current densities.

Remarkable progress has been made in recent years in terms of CO_2RR selectivity and partial current density. This is particularly true for CO-production, which is very close to meet the industrial requirements.[20,34] Our group was the first to reach 1 A cm^{-2} partial current density for CO formation, while maintaining high selectivity, conversion and low cell voltage in a zero-gap electrolyzer by applying a PiperIon membrane, which possesses a high carbonate ion conductance.[20] Stable operation, exceeding 1000 h,[34,35] has also been reported for CO_2 to CO electroconversion; however there seems to be a trade-off between partial current density/selectivity and long-term operation.[27] A recent roadmap on CO_2RR highlighted that CO and ethanol could be the ideal products of electrochemical CO_2 reduction, taking into account the market size, as well as the cost- and emission reduction when changing from current petrochemical production to electrosynthesis.[36,37] CO can be upgraded to a wealth of products, such as transportation fuels through the Fischer–Tropsch process,[38] and can also be electrochemically further reduced to C_{2+} products (CORR).[38] The latter holds greater promise compared to the direct $CO_2 \rightarrow C_{2+}$ conversion, considering energy efficiency and system design

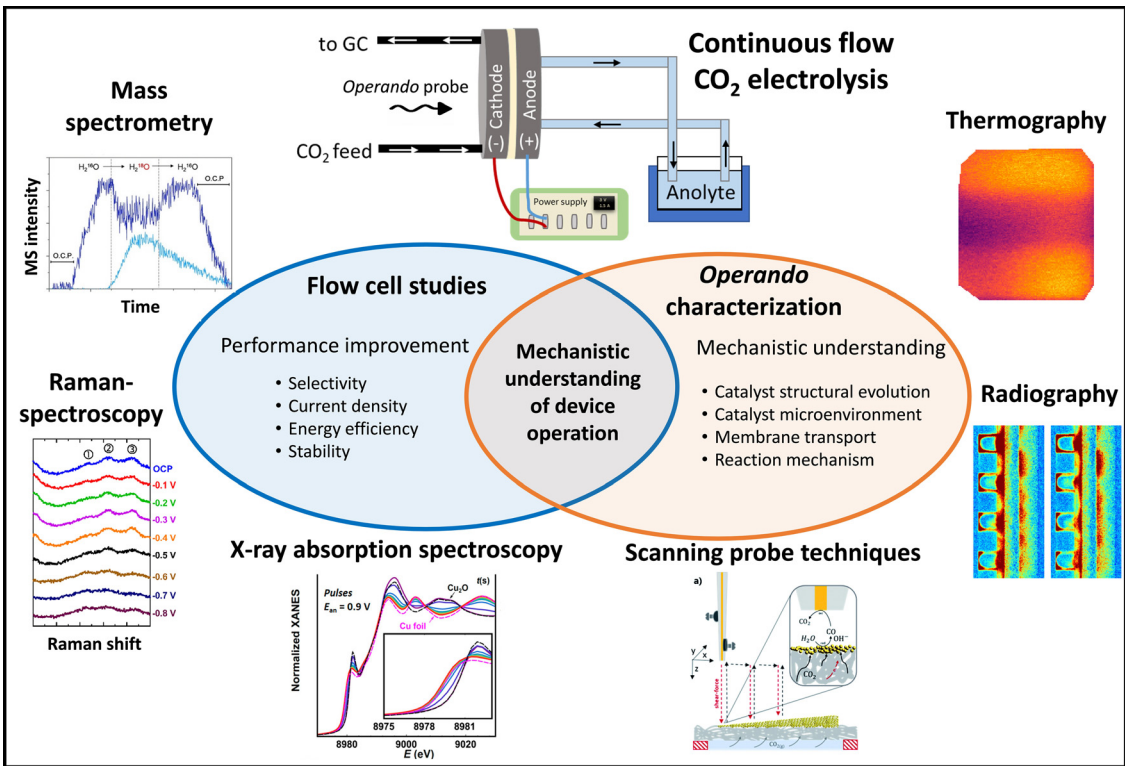

Fig. 1 Combining continuous flow CO_2 electrolysis with *operando* characterization. Reproduced from ref. 81, 100, 118, 125, 130 and 136 with permission from the copyright holders. Minor modifications have been made without altering the meaning of the original content.

(carbonate-free operation). Interestingly, the highest current densities were reported for C_{2+} product formation[21,27,39,40] in CO_2RR. The high initial performance, however, was usually followed by quick deactivation, which may be attributed to

Table 1 Comparison of electrolysis conditions and role of specific cell components in batch and flow CO_2 electrolyzers

	Batch (H-type) cell	Flow cell
Achievable CO_2RR current density[20,21,24,27]	< 50 mA cm^{-2}	>1 A cm^{-2}
Reactant	Dissolved CO_2/bicarbonate	Gas-phase/dissolved CO_2
Diffusion length of CO_2[24,43,44,47]	$\sim$50 μm	$\sim$50 nm
Catholyte	$MHCO_3$[a]	MOH, $MHCO_3$, none
Local pH at the cathode[48–53]	Near-neutral or alkaline	Alkaline
pH gradient[48–53]	$pH_{surface} > pH_{bulk}$ (up to 5 pH unit difference)	Bicarbonate electrolyte: $pH_{surface} > pH_{bulk}$, alkaline electrolyte: $pH_{surface} < pH_{bulk}$
Catalyst support[6,54–57]	Flat (glassy carbon, metal foil) or porous (carbon paper, metal foam)	Porous (carbon paper, metal foam, PTFE)
Ionomer[16,29,58]	Not mandatory, mainly catalyst binder, but can change morphology, surface chemistry	Microfluidic: same role as for H-cell; zero-gap: ensures ionic conductance
Membrane[59]	Type: CEM/AEM; role: product separation; does not limit cell performance	Type: CEM/AEM/BPM[b]/none; role: product separation, in zero-gap-cells it determines catalyst surface chemistry; can limit cell performance
Surface concentration of reactants/intermediates[24]	Lower	Higher
Electrode configuration	3-Electrode, cathode potential	2 or 3-electrode, full cell voltage/cathode potential

[a] M: alkali metal cation. [b] CEM: cation exchange membrane, AEM: anion exchange membrane, BPM: bipolar membrane.

catalyst restructuration/degradation or cell failure caused by either flooding or salt precipitation. For instance, a F- and K-modified Cu-catalyst showed a maximum of 53% FE for ethanol at a current density as high as 423 mA cm^{-2} recently; however, the longest reported performance test lasted only 12 hours with much lower (<20%) ethanol FE, which is still far from industrial relevance.[41] We think that *operando* characterization will be a key tool to understand such performance loss mechanisms (Fig. 1).

Batch *versus* flow electrolysis

In this section, we compare the conditions that prevail and the role of different cell components during CO_2RR under low (H-type cells) and high (flow cells) current density conditions (Table 1). We aim to highlight how these different configurations, thus reaction environments, might influence reaction mechanisms and *operando* characterization tools under practically relevant conditions. In H-type cells, CO_2 reaches the catalyst in the liquid-phase (*i.e.*, dissolved in the electrolyte), which limits the maximum CO_2RR current density (*ca.* to < 50 mA cm^{-2} for CO formation), because of the low solubility of CO_2 in aqueous-electrolytes (*ca.* 30 mM).[24] In contrast, in flow cells accommodating GDEs, gas-phase CO_2 flow reaches the catalyst, significantly increasing the CO_2 availability. Although the presence of a real three-phase boundary layer (gas–liquid–solid) has been debated,[24,43] even if a thin electrolyte layer covers the active catalyst phase, the diffusion length for CO_2 in GDE-based cells is at least one order of magnitude lower compared to that in batch cells.[24] In H-type cells, bicarbonate electrolytes are almost exclusively used, as they can serve as a stock for CO_2, increasing its effective concentration at the electrode, as demonstrated previously for both metal[44] and carbon-based[45] electrodes. As flow cells are not limited by CO_2 solubility, they allow for the use of a much wider range of electrolytes.[46] Hereby, the often-reported promotion of CO_2RR by electrolyte components can be fully harnessed. Furthermore, the flow cell configuration can also assist mechanistic understanding, by allowing for a larger variability of experimental parameters,[60] such as fluid flow rates or reactant compositions (gas mixtures), which can be better understood if combined with *operando* characterization.

The use of alkaline electrolytes is widespread in flow CO_2RR, because of the reduced CO_2RR overpotentials, suppressed HER rates, and enhanced C_{2+} product formation in these environments.[21,61] Performing CO_2RR in strongly alkaline electrolytes in H-type cells, however, is not possible because the acid–base reaction between dissolved CO_2 and OH^- leads to significant pH decrease. As a consequence of the different electrolyte environments in flow and batch cells, the local pH may also differ in the two scenarios, influencing catalyst performance. A few studies reported local pH measurements during CO_2RR by surface-enhanced infrared spectroscopy (ATR-SEIRAS),[48,62] rotating ring disc (RRDE) voltammetry[49] or scanning electrochemical microscopy (SECM)[63] in batch configurations, and revealed notably (up to 5 units) higher pH near the electrode surface, compared to the bulk solution (Fig. 2(A) and (B)). This

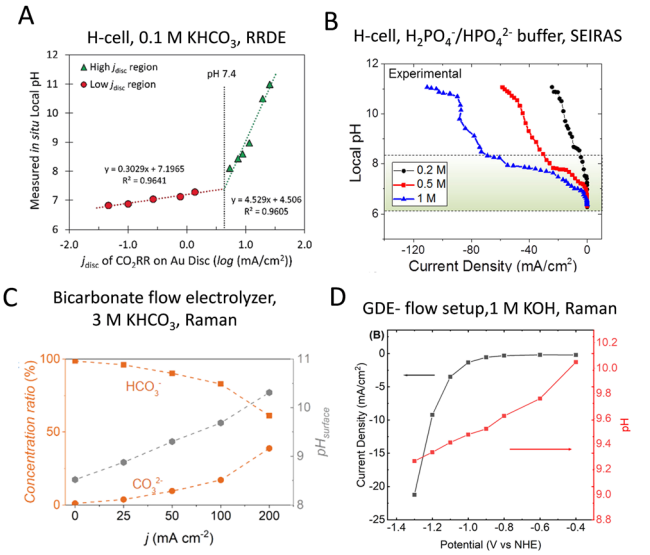

Fig. 2 Experimentally determined pH values at the catalyst surface in different cell configurations and electrolytes. (A) Local pH at the surface of a gold catalyst in a CO_2-saturated $KHCO_3$ electrolyte, determined by rotating ring disc voltammetry. Reproduced from ref. 49 with permission from John Wiley and Sons. (B) Surface pH of a copper electrode in contact with CO_2-saturated phosphate buffers determined by surface-enhanced infrared spectroscopy. Reproduced from ref. 62. Copyright 2019 ACS. (C) Local pH measurements in a continuous-flow bicarbonate electrolyzer with a silver foam cathode by Raman spectroscopy. Reproduced from ref. 51. Copyright 2020 ACS. (D) Local pH measurements with Raman spectroscopy on the surface of a Cu GDE in contact with a flowing 1 M KOH electrolyte and gas-phase CO_2. Reproduced from ref. 52. Copyright 2020 ACS.

local pH variation can be attributed to the production of OH^- (or consumption of H^+) in both CO_2RR and HER. It was found consistently that the surface pH (*i.e.*, pH at the catalyst surface) is higher than the bulk pH of the electrolyte (*i.e.*, pH at distances from the electrode surface larger than the diffusion layer thickness) during CO_2RR when using bicarbonate electrolytes in both H-type and flow cells (Fig. 2(A) and (C)).[48–51] During alkaline flow electrolysis, however, the neutralization reaction between CO_2 and OH^- can counterbalance the increase in the local pH (caused by the faradaic reactions), resulting in lower surface pH compared to the bulk electrolyte (Fig. 2(D)).[52,53] This acid–base reaction can also be detrimental for electrolyzer operation if carbonate precipitates are formed.[22,61,64] Additionally, the fluid streams in flow setups may also influence the local pH, either because of the continuous electrolyte refreshment or the change in the rate of CO_2 + OH^- reaction when the gas/electrolyte flow rates are varied.[53]

Electrolyte flow, in principle, can be advantageous for *operando* experiments, helping the removal of gas bubbles from the electrode surface which usually makes spectroscopic data collection challenging.[12] Gas bubbles sticking to the electrode can also result in severe potential variations along the electrode surface,[65] causing local activity changes. The porous, gas permeable structure of GDLs can mitigate this issue; however, their use also limits the implementation of certain *operando* techniques. For instance, FTIR spectroscopy (to detect surface

adsorbates) cannot be performed in the more surface-sensitive ATR (internal reflection) configuration on GDEs, because it requires the deposition of a very thin catalyst layer on the surface of an ATR crystal.[13,62,66] To mimic flow cell conditions, only external reflection (IRAS) can come into consideration, with an ultrathin electrolyte layer between the IR transparent window and the catalyst.[13,67] This would come, however, at the expense of decreased surface sensitivity with additional technical challenges (reduced time resolution, solvent bands),[13] which explains why *operando* IR spectroscopy has not been implemented in GDE-setups yet. On the other hand, carbon-based GDLs are particularly advantageous for *operando* X-ray absorption (XAS), as the relatively thin (few hundred μm) carbon papers are transparent for hard X-rays, as opposed to metal or thicker glassy carbon substrates commonly employed for H-cell studies.[12]

Apart from the catalyst microenvironment, it is also worth to compare the role of particular cell components in batch and flow electrolysis. To start with the core constituent, in principle the same or similar catalyst materials can be used in both setups. Nevertheless, the optimal reaction conditions can be substantially different in the two configurations; therefore catalysts have to be optimized for the two types of measurements separately. For instance, while HER dominated on Cu nanocatalysts in an H-type cell, when performing CO_2RR using the same catalysts in an alkaline flow electrolyzer, FE_{H2} was largely suppressed with the concomitant increase in the FE for C_{2+} products (Fig. 3).[17] Another example can be the case of nickel–nitrogen doped carbons, often outperforming metal catalysts in terms of CO production rate in H-cells and CO formation FE in flow cells, but their maximum reported stability was limited to a few tenth of hours in flow cells,[68,69] because of rapid flooding at high current densities (note the similarity of the carbon skeleton to the carbon paper supports). One also has to consider which performance metric is in the focus of interest (*e.g.*, selectivity, current density, energy- or CO_2 conversion efficiency) as different system design rules might apply for the optimization of each.[60]

Notably, flow cells bear higher experimental complexity, as several other processes other than the kinetics of cathode half reaction can limit their performance at high reaction rates, such as the paired anode process,[27,70] the ionic conductivity of the membrane, or GDE flooding.[20] Furthermore, the determination of the individual electrode potential is not always straightforward at high currents and particularly in zero-gap devices.[71,72] Therefore, when we aim to correlate the catalyst structure/microenvironment in a flow electrolyzer to its performance using *operando* spectroscopy, we have to make sure that it is not limited by other factors.

Membranes are primarily used to separate the anode and cathode compartments of the cells, and therefore to inhibit product crossover. Moreover, they transport water and ions between the two half-cells and determine the type of ionic charge carriers (anions/cations) and the direction of their movement in the cell.[59] In zero-gap devices, where the catalysts are in direct contact with the membrane, they control the microenvironment (*e.g.*, pH and near-surface components) and thus the surface chemistry of the catalysts. Furthermore, they can also significantly influence the water management in the cell.[73] Because of this, the catalyst layer should be preferably characterized together with the membrane; therefore the development of *in situ*/*operando* techniques for the characterization of full zero-gap devices or MEAs[30] should be urgently promoted. The above effects are less pronounced in H-type cells and microfluidic flow cells, because of the presence of buffering electrolyte layers. The ionomer besides acting as a catalyst binder can also modify the catalyst microenvironment and morphology, moreover can also actively participate in the CO_2RR/CORR by interacting with reactants or intermediates.[29,74] In the MEA case, it also ensures ionic conduction between the catalyst particles as well as between the catalyst and the membrane.

Challenges in continuous flow CO_2 electrolysis and how *operando* spectroscopy can overcome these

Before summarizing the existing reports on *operando* characterization of continuous-flow CO_2 electrolyzers, we would like to give a brief overview of the main challenges associated with this rising technology. We also underscore how *operando* characterization can

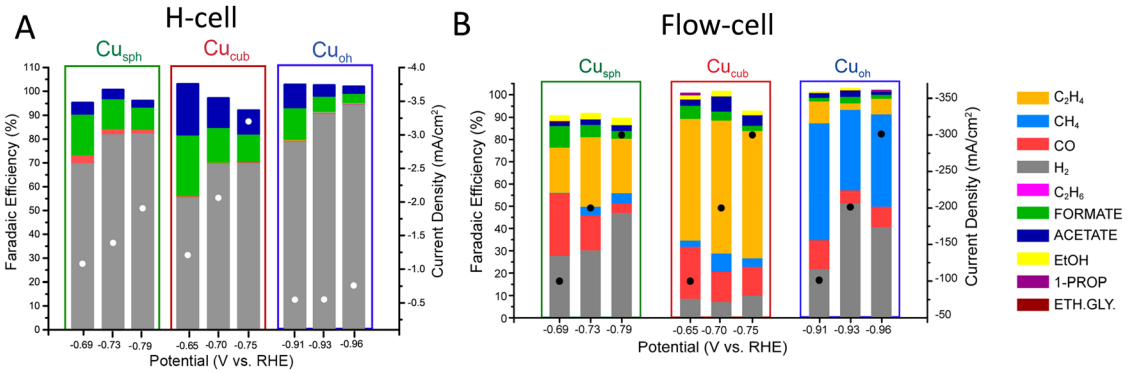

Fig. 3 Selectivity of the same Cu nanocatalysts in an H-cell using a CO_2-saturated 0.1 M $KHCO_3$ electrolyte (A) and in a gas-fed microfluidic flow cell with a flowing 1 M KOH electrolyte (B). Reproduced from ref. 17. Copyright 2020 ACS.

be a tool to help overcome these challenges (Table 2). Keeping the overall energy consumption of the cell as low as possible is one of the main goals from an economic point of view. The energy efficiency is directly related to the cell voltage, which is the sum of the anodic and cathodic half-cell voltages and ohmic losses originating from the membrane and electrolyte layers (if present). From a materials-science perspective, developing new catalysts with reduced overpotential towards the desired product is the most straightforward way to reduce the energy consumption.[7,75,76] Finding alternative catalysts (*e.g.*, bimetallics) or increasing the abundance of specific structural motifs or crystal facets[17] selectively producing certain products are strategies to overcome the above-mentioned limitation. *Operando* spectroscopy, providing information on the catalyst bulk or surface structure (*e.g.*, XAS, XPS, Raman), has largely contributed to catalyst improvement[5,6,85] already, and will continue to do so hopefully under practically relevant conditions too. For a fixed anodic and cathodic reaction pair, however, we cannot go below the thermodynamic cell voltage, which is 1.33 V for CO production coupled with the anodic OER.[77,86] Nevertheless, this value can be lowered to more than 1 V when using alternative anode reactions, for instance the increasingly studied glycerol oxidation.[77,87]

A significant portion of the energy input in flow electrolyzers can be lost at the membrane[71,88] (Fig. 4(B)), because of its low ionic conductivity. As carbonate and bicarbonate ions were identified as main charge carriers in AEM CO_2 electrolyzers[20,89] (Fig. 4(A)), producing membranes that possess high conductivity for these ions is a prerequisite for further development. The water uptake of the membrane also significantly influences its ionic conductivity,[31] which can be studied by neutron or X-ray radiography during electrolyzer operation.[78,90,91] These techniques therefore have the potential to identify reasons for ohmic losses in CO_2 electrolyzers.

The experimental conditions can have significant influence on the formation of multicarbon products. High local pH[79] and intermediate surface CO concentration[80] were found to be beneficial for C–C coupling, while suppressing the competitive HER and methane formation. To understand how these parameters affect reaction mechanisms, at high current densities, *operando* local pH measurements and Raman/IR spectroscopy (to detect surface CO_2/CO concentrations) should be implemented in GDE-setups too. In addition, electrochemical mass spectrometry with isotopic labeling can also largely contribute to our understanding of mechanistic pathways towards certain products. Last but not least, reduction of CO has several benefits compared to CO_2 reduction, such as the lower overpotential for C_{2+} products,[92] higher near-surface CO concentration, and the absence of carbonate formation in alkaline electrolytes.[93] As cell designs for CO and CO_2 reduction are very alike, *operando* methods can be similarly implemented in CO electrolyzers as well giving additional insights into C–C coupling under high current density conditions.

Several degradation mechanisms can lead to unstable electrolyzer performance, such as GDE flooding, formation of carbonate precipitates, catalyst deactivation, and membrane degradation. The most commonly employed gas diffusion layers (GDLs) are carbon-based ones (*i.e.*, carbon paper or cloth). One of the major obstacles when using these supports is their tendency to lose their hydrophobicity which consequently leads to the domination of the competing hydrogen evolution reaction (HER), resulting in flooding.[94] In flow cells with electrolyte layers, flooding usually occurs even after a few hours (if not less) of operation,[94] largely reducing the lifetime. To mitigate this issue, PTFE-based GDLs or

Table 2 Main challenges of continuous-flow CO_2 electrolysis and strategies to overcome these. The third column lists the main *operando* methods expected to contribute

Challenges	Strategies to meet the challenge	Contribution of *operando* characterization
Improving energy efficiency[5,6,59,77,78]	• Lowering anode and cathode potentials ○ More active catalysts ○ Alternative anode reactions	• XAS[a], XPS[a], Raman
	• Improving membrane conductivity	• Radiography, EIS[a]
Production of multi-carbon molecules[4,79–81]	• Novel catalyst materials • Active site stabilization	• XAS, XPS, Raman
	• Optimization of local pH, CO_2/CO concentration	• Local pH, Raman, IR
	• Mechanistic understanding of C–C coupling • CO reduction	• Raman, IR, EC-MS[a]
Stability improvement (>1000 h)[22,59,82]	• Wet-proof GDEs	• Radiography
	• Mitigating carbonate formation	• Local pH and ion concentration measurements
	• Improving membrane durability	• IR, Raman
Efficient CO_2 utilization[23,83]	• Mitigation of CO_2 and product crossover	• Radiography • Local detection of CO_2 and products
Scaling-up[55,84]	• Scale-up or scale-out	• Local measurement of reactant/product concentrations, temperature, humidity (distribution)

[a] XAS: X-ray absorption spectroscopy, XPS: X-ray photoelectron spectroscopy, EIS: electrochemical impedance spectroscopy, EC-MS: electrochemical mass spectrometry.

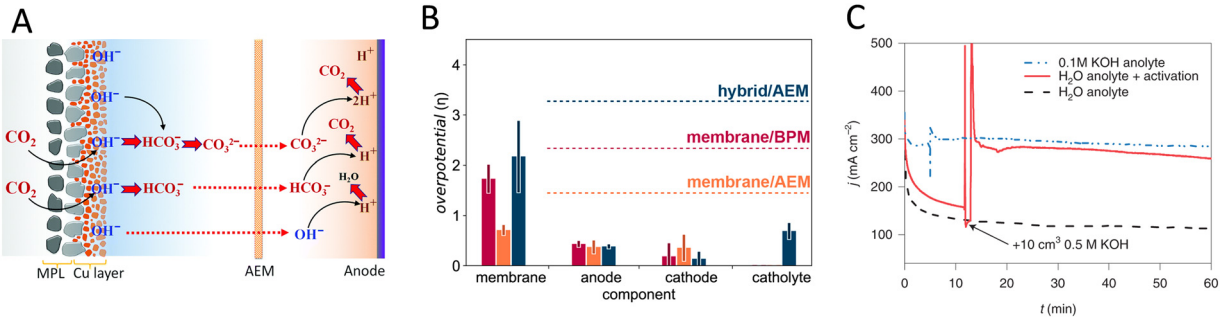

Fig. 4 (A) Proposed carbon balance paths in an AEM electrolyzer with a flowing $KHCO_3$ electrolyte. Reproduced from ref. 89. Copyright 2020 RSC. (B) Overpotentials during CO_2RR at 200 mA cm^{-2} for each of the functional components in membrane/BPM (red), membrane/AEM (orange), and hybrid/AEM (navy) electrolyzers. Values were determined by using an analytical flow cell capable of resolving voltage drops across individual electrode and membrane components during CO_2RR. Reproduced from ref. 71. Copyright 2019 ACS. (C) Alkali metal ion "activation" of an AEM CO_2 electrolyzer operated with a pure water anolyte. Reproduced from ref. 22. Copyright 2021, the Author(s), under exclusive licence to Springer Nature Limited.

metal foams are being investigated, but no breakthrough has been achieved so far. Nevertheless, the properties of the GDLs (thickness, porosity, PTFE content) largely influence the CO_2RR performance, as demonstrated in others and our recent work too.[42] The formation of (bi)carbonate precipitates under locally alkaline conditions (AEM electrolyzers) can also accelerate GDE flooding.[95] Moreover, these precipitates block the transport of CO_2 to the catalyst active sites too.[22] This is a major hurdle particularly in zero-gap devices, because the thin electrolyte layer covering the catalyst can easily become saturated with these salts. Periodic rinsing of the cathode with water[55] or pulsing the potential[64] were two approaches suggested to mitigate this problem.

Operating zero-gap AEM CO_2 electrolyzers with a pure water anolyte would be highly desired, as the absence of alkali cations in the system would inherently circumvent precipitate formation, in addition to the advantage of eliminating the use of expensive and dangerous alkali hydroxides. Our group recently showed that high performance water-based operation is only possible when small amounts of alkali cations (*i.e.*, K^+ or Cs^+) are present near the cathode (Fig. 4(C)).[22] Although the exact mechanism of their participation in the CO_2 electrolysis is not clear yet, this coincides with the observed promotional effect of cations in CO_2RR under batch electrolysis conditions.[96–99]

The aforementioned cell failure mechanisms are closely connected to the water management of the cell; thus their mitigation can be assisted by *operando* techniques that can give direct evidence on the relative humidity conditions or water content of the cell components. In this sense, radiographic analysis[78,91,100] or the incorporation of relative humidity and temperature sensors in the electrolyzers[73] are expected to contribute with novel insights. Additionally, methods that can locally measure the metal ion concentrations in the vicinity of the GDEs would also be highly desired.

Much less attention has been paid to possible membrane degradation mechanisms in CO_2/CO electrolyzers.[59] In general, CEMs have around one order of magnitude higher proven operational lifetimes compared to AEMs.[101] One degradation mechanism of AEMs includes the nucleophilic attack of OH^- on the cation functional groups and the polymeric backbone of the membrane, especially when they are not fully hydrated.[102] Moreover, the formation of liquid products, such as ethanol, can also accelerate AEM degradation.[59] In the future, more works should aim at both the post-mortem and *in situ*/*operando* characterization of ion exchange membranes,[103,104] although the latter can be experimentally extremely challenging.

AEM CO_2 electrolyzers suffer from significant loss of CO_2 at the anode, because of the transport of carbonate and bicarbonate through the membrane, reducing carbon efficiency (Fig. 4(A)). CO_2 electrolysis in an acidic cathode environment (*e.g.*, using CEMs) could overcome this issue, but it generally results in low CO_2RR selectivity, because of the favored HER. Recently, under certain experimental conditions, however, CO_2 was reduced with high selectivity to CO and even to C_{2+} products in acidic electrolyzers. A common feature of these works was the abundance of weakly hydrated alkali metal cations (K^+ or Cs^+) in close proximity of the cathode.[39,105–107] This finding may lay down a new research path for acidic CO_2 utilization, which could largely benefit from *operando* characterization uncovering the local cathode microenvironment. Not only CO_2, but also liquid products may cross the membrane, which is particularly significant for anionic species in AEM CO_2 electrolyzers.[108] This, on the one hand, inhibits precise FE calculations if not properly accounted for, and on the other hand results in extra downstream separation costs. Local and real-time detection of CO_2RR products in the cathode vicinity is one possibility to mitigate the issue with performance assessment, but the challenges associated with detecting non-volatile liquid products using electrochemical mass spectrometry should be noted.[109] A better and universal solution would be the development of AEM membranes with functional groups blocking the movement of all liquid products. Tuning the membrane water volume fraction was also found to be a useful strategy to reduce product crossover.[110]

Last, but not least, scaling up of CO_2/CO electrolyzers is associated with several challenges (such as fluid- and heat management). One very promising scale-up strategy is the construction of large size and multi-cell stacks, as for fuel cells and water electrolyzers. Such cell stacks were already demonstrated for CO_2 electrolyzers both with and without a liquid catholyte,[55,111–113] including our pioneering work for a zero-gap architecture.[55] As the size of the cell and the number of cell stacks increase, significant local variations in the different

operational parameters within the device can be expected. For instance, CO_2 concentration gradients can develop within large cells, particularly at high CO_2 conversion rates. This can shift the selectivity towards HER; therefore measurement of reactant and product concentrations at different positions of the cell might be required. Similarly, mapping the temperature and relative humidity during operation can also become necessary by placing sensors inside the electrolyzer or using other methods, such as thermography. These data can additionally serve as inputs for multi-physics modeling which can help to identify optimal operational parameters and support technological development.

Operando characterization of CO_2 electrolyzers

Table 3 summarizes the existing *operando* techniques in continuous-flow CO_2 reduction with their main advantages and limitations. In the following subsections we give an overview of these focusing on what kind of information can be deduced from these measurements.

X-ray absorption spectroscopy

X-ray absorption spectroscopy is a core-level X-ray technique, measuring the X-ray absorption coefficient as a function of energy.[114] It is element-specific, and suitable for the investigation of a wide range of materials including ordered, disordered, amorphous or even liquid-phase ones. Unlike X-ray photoelectron spectroscopy, it does not require high vacuum conditions; therefore it is excellently suited for *operando* measurements of electrocatalysts, reviewed recently.[12] Nevertheless, to reach high signal to noise ratios, thus to allow for extraction of high quality data, usually synchrotron irradiation (high flux of high energy X-rays) is needed. The measured spectra can be divided into two regions.[12] The XANES (X-ray absorption near edge structure) region is located in the vicinity of the absorption

Table 3 Summary of *operando* techniques applied to continuous-flow CO_2 electrolyzers

Operando technique	Information content/main advantages	Main limitations	Time resolution	Spatial resolution
XAS[a] [18,113,115,117,119–123]	• Catalyst structure (oxidation state, coordination environment) • Only minor cell modification needed	• Bulk sensitive • Synchrotron irradiation	• Typically 20–30 minutes • Subseconds for QXAFS	N/A
Raman spectroscopy[51,52,124,125]	• Catalyst structure (oxidation state) • Adsorbed intermediates/products • Local pH with spatial resolution • Widely available at lab-scale	• SERS effect only on certain metal nanostructures • Less suitable for zero-gap design	• Few tenths of seconds	• μm-scale (x^b)
Fluorescent microscopy[50]	• Local pH measurement with spatial resolution in the x, y, z direction • pH measurement within catalyst trenches	• Fluorescent probe added to the electrolyte might change the local reaction environment	N/A	• μm- scale (x, y, z^b)
UV-Vis spectroscopy[30]	• pH measurement at the catalyst/membrane interface (MEA-design)	• Significantly different cell design compared to the real device (*in situ*)	N/A	• nm-scale (z)
SECM[a]	• Local reactivity and local pH • Spatially resolved activity maps	• Low achievable current densities	N/A	• μm-scale (x, y)
AFM[126 a]	• High resolution topography and mechanical property maps	• Small scan size • Rapid flooding at high currents	• Few minutes	• Few tenths/hundreds of nm
MS[81,127 a]	• Real-time detection of products/intermediates with low detection limit • Mechanistic information • Isotopic information	• Deconvolution of signals (*e.g.*, CO, CO_2) can be challenging	• Seconds/tenths of seconds	N/A
Neutron/X-ray radiography[78,91,100,128,129]	• Water management • Gas evolution • Precipitate formation • *Operando* cell failure diagnostics • Only minor cell modification needed	• Neutron/synchrotron facility • Limited elemental information	• Few seconds for X-ray few tenths of seconds for neutron	• μm – scale (x, y)
Thermography[130]	• Local activity mapping • Noninvasive probing to assess activity distribution	• One-to-one correlation between temperature change and activity has to be proved	• Depends on catalyst substrate, layer thickness, *etc.*	

[a] XAS: X-ray absorption spectroscopy, SECM: scanning electrochemical microscopy, AFM: atomic force microscopy, MS: mass spectrometry. [b] x and y are directions in the plane of the GDE, while z is perpendicular to that.

edge, and provides information on the chemical state of the absorbing atoms, local symmetry, and chemical bonding. The EXAFS (extended X-ray absorption fine structure) region, covering a range of up to a few thousand eV above the absorption edge, is sensitive to the arrangements of nearest neighbors around the absorbing atom, such as interatomic distances and coordination numbers. One limitation is its bulk-averaging nature, which must be kept in mind when studying electrocatalysts. This can be mitigated in part by measuring thin catalyst layers,[115] provided that this enables sufficient signal intensity. Furthermore, recording an XAS spectrum typically takes 20–30 minutes, which impedes tracking fast processes. At some specialized beamlines, however, the quick-XAFS (QXAFS) method is available, allowing for time-resolution in the millisecond range.[5,116–118]

X-ray absorption spectroscopy is currently the most widely applied *operando* spectroscopy to study the evolution of catalyst structure during CO_2RR under high current density conditions.[18,113,115,118–123] Because of its great compatibility with flow cell designs, the *operando* measurement requires only minor cell modifications (Fig. 5). The absence of electrolyte in the beam path when measuring in the back-illumination fluorescence mode eliminates complications associated with gas bubble formation in the electrolyte. Flooding or electrolyte perspiration through the pores of the GDE can, however, be detrimental for the measurement. To allow for the X-ray beam to pass through the cell body (usually made of metal or plastic), most frequently a polyimide window is cut into the cathode end plate and flow field. This, however, can disrupt the flow field (thus reactant transport), possibly resulting in performance variations compared to the unmodified cell. In the fuel cell field, the application of thinned graphite flow-fields, which are transparent to X-rays and have identical geometry as the flow-field in the original cell, has been reported.[131–133] This design may be adopted in the future for CO_2 electrolyzers as well, creating a more representative environment for *operando* tests.

Different copper catalysts have been investigated by *operando* flow cell XAS in recent years.[113,115,118–120] In one work, the effect of electrolyte, applied current density, and catalyst layer thickness was studied on a sputtered Cu cathode.[115] No obvious changes were found for a 100 nm thick Cu catalyst layer when tested at different current densities (1 and 100 mA cm^{-2}) in a $KHCO_3$ electrolyte: in both cases only metallic Cu was present during CO_2RR. Based on the determined Cu–Cu interatomic distances and Debye–Waller factors (measure of disorder in the crystal lattice), higher disorder was found for the 20 nm thick sample, compared to the 100 nm one under reaction conditions (100 mA cm^{-2}), which seemed to be less favorable for C_{2+} product formation. In another work, a KOH-incorporated Cu catalyst (Cu–KOH) was tested by *operando* XAS in a zero-gap device.[113] This catalyst, consisting of fully oxidized copper species (Cu^{2+}) in the as-prepared state, showed improved performance for ethylene production (54.5% FE, 153 mA cm^{-2}) compared to the reference Cu black, Cu_2O and CuO samples. *Operando* XAS measurements revealed that although the material was reduced to a large extent to Cu^0 during CO_2RR (E_{cell} = 2.5–4 V), minor amounts of oxidized Cu species survived under the harsh reducing conditions. The Cu–KOH electrode contained a higher fraction of $Cu(OH)_2$ compared to the reference Cu black, which was explained by its special (echinoid-shaped) morphology and defect-rich structure originating from the KOH incorporation. The high density of defect sites most probably induced a local pH increase, and resulted in the partial re-oxidation of the metallic Cu during CO_2RR. The synergy between remaining Cu_2O, $Cu(OH)_2$ and metallic Cu was considered to be responsible for the improved ethylene selectivity. In contrast to the latter finding, full reduction of a $Cu(OH)_2$ catalyst to metallic Cu was reported in a microfluidic *operando* XAS flow cell after 1 hour of reduction,[120] possibly indicating that the different catalyst environments in microfluidic *vs.* zero-gap devices can affect the reducibility of Cu.

Pulsed CO_2RR (p-CO_2RR) was found to be an easy, yet versatile technique to steer the selectivity of copper catalysts, because of the unique changes induced in the catalyst structure, its microenvironment and the electric double layer when pulsing the potential.[117] In this dynamic reaction environment, only *operando* techniques are able to provide mechanistic insights. In this regard, QXAFS with second/subsecond time resolution is a key tool to follow changes in the catalyst structure even during individual pulses[117,118] (Fig. 6). Pulsed CO_2RR was recently applied to a Cu nanocube catalyst in a microfluidic flow cell, and it was found that the C_2/C_1 selectivity can be tuned by adjusting anodic potential (E_a) while fixing the cathodic value (E_c).[118] While at E_a = 0.9 V (*vs.* RHE), the selectivity towards C_{2+} products slightly increased compared to the potentiostatic reduction, higher E_a values (*i.e.*, 1.2 V) favored CH_4 formation over C_2H_4. *Operando* QXAFS revealed gradual reduction of the dominating Cu_2O phase in the as-prepared catalyst to Cu^0 during static reduction, as well as under pulsed conditions with lower E_a (Fig. 6(A)). Even though metallic Cu re-oxidized to Cu^+ during the anodic pulse (Fig. 6(B)), its much faster reduction during the cathodic pulse resulted in a net reduction of the catalyst over time (Fig. 6(A)). With the higher anodic potential (E_a = 1.2 V), a small fraction of Cu^{2+} also appeared at the initial stage of CO_2RR, but its concentration rapidly dropped to zero (conversion back to Cu^+). In this case, a significant fraction of Cu^+ remained intact (*ca.* 30%) for the whole duration of the experiment. These findings were complemented with the more surface sensitive SERS, which also confirmed the accumulation of Cu_2O when

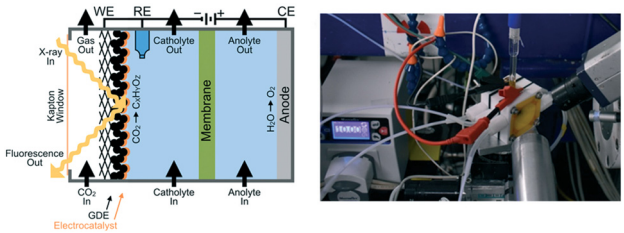

Fig. 5 Schematic illustration and photograph of a microfluidic *operando* XAS cell allowing for fluorescence measurements. Reproduced from ref. 115. Copyright 2020 RSC.

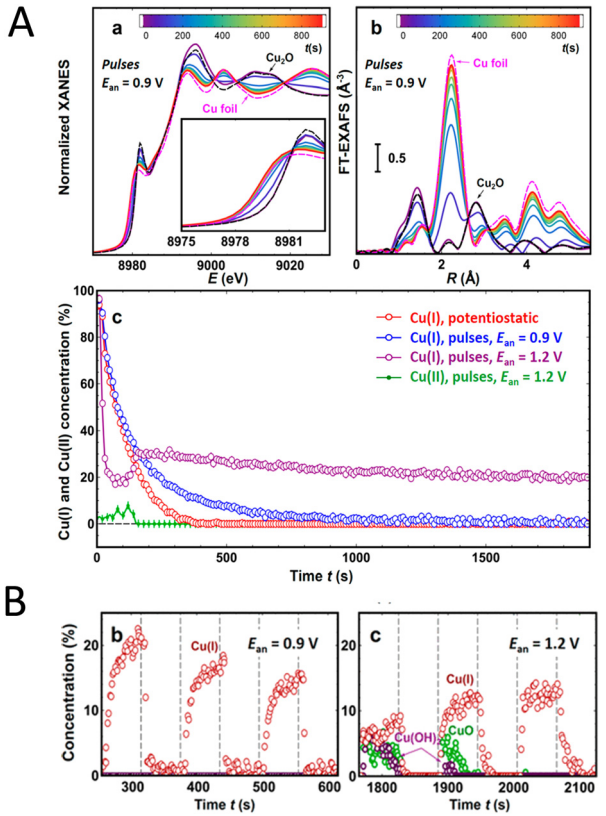

Fig. 6 (A) Time-dependent XANES and FT-EXAFS spectra at the Cu K-edge during pulsed CO_2RR on Cu nanocube catalysts. Results of the linear combination XANES fitting under potentiostatic and pulsed reduction. (B) Periodic oxidation and reduction of the pre-reduced catalysts followed by QXAFS during individual (60 s) pulses. Reproduced from ref. 118. Copyright 2021 the Authors, published by ACS.

pulsing with E_a = 1.2 V, originating from the reaction between metallic Cu and OH^- ions during an anodic pulse.

Operando QXAFS was also employed to study alloying processes in bimetallic catalysts during CO_2RR, revealing active phases responsible for certain products. Zn-decorated Cu_2O nanocubes with varying Zn-contents were investigated at current densities up to 500 mA cm^{-2} in a microfluidic flow cell.[119] While the pure Cu_2O exhibited high FE for C_2 products (41% C_2H_4 and 12% EtOH at −500 mA cm^{-2}), the increase in Zn-content resulted in a gradual enhancement of the CO selectivity (from 18 to 53%) and a decrease in C_{2+} products. The *operando* measurements revealed that most of the Cu^+ (Cu_2O) and Zn^{2+} (disordered ZnO) species in the as-prepared catalysts were reduced to the respective metallic states within 60 s. Linear combination analysis (LCA) of the XANES data suggested faster reduction of Zn^{2+} than Cu^+, and revealed that the presence of Zn stabilizes Cu^+ during CO_2RR. The quick reduction of Cu^{2+} and Zn^{2+} was followed by a gradual and significantly slower transformation of the Cu and Zn phases into Cu_xZn_y alloys, which coincided with a time-dependent change in selectivity. Neural-network (NN) EXAFS analysis further uncovered that an increasingly Cu-rich (fcc-type) structure is formed at longer reaction times and that the contribution of a non-fcc type (Zn-rich) alloy is higher at higher initial Zn contents. QXAFS in combination with LCA-XANES and NN-EXAFS analysis was used to correlate redox peaks on the cyclic voltammograms of the bimetallic samples with the chemical evolution of Cu and Zn species, albeit at low current densities. This was complemented with *operando* SERS to deconvolute surface and sub-surface changes. These investigations revealed easier reduction of Cu^+ located at the surface than in the bulk, and showed that the reduction peak of bulk Cu^+ positively shifts in the presence of Zn (in a Cu–Zn alloy). The latter works nicely demonstrated the rich information content of *operando* XAS measurements when combined with advanced data analysis (machine learning) and complementary surface-sensitive techniques.[118,119]

Silver is the state-of-the-art catalyst for CO_2 reduction to CO, but interestingly only a couple of studies aimed at its *operando* XAS investigation at high current densities.[115,122] A sputtered Ag catalyst was studied in a microfluidic flow cell at current densities between 1 and 200 mA cm^{-2}.[115] An increase in crystallite size and a decrease in Ag–Ag distance during CO_2RR were found, compared to the as-prepared (*ex situ*) sample. At higher current densities ($\geq$100 mA cm^{-2}), the presence of Ag–O bonds was also identified. Silver dendrites grown on a W seed were found to be efficient catalysts, showing 400 mA cm^{-2} CO partial current density in a zero-gap AEM electrolyzer.[122] The structure of the catalyst was studied by *operando* XANES and depth resolved XPS measurements, which revealed residual Ag^+ species ($Ag_xC_yO_z$) in the near-surface region under CO_2RR conditions. The authors assumed that the large number of defects and undercoordinated Ag on the Ag-dendrite branches resulted in enhanced electric fields, which reduced the thermodynamic barrier for CO_2RR and resulted in improved performance compared to the Ag/C benchmark.

With the aim to develop low-cost and earth-abundant catalysts for the conversion of CO_2 into CO, Zn-based catalysts are being researched. A zinc pyrophosphate ($Zn_2P_2O_7$) (pre)catalyst delivered up to 441 mA cm^{-2} current density for CO production at a low potential (−0.87 V *vs.* RHE), with this being among the best Zn-based CO_2RR catalysts. The excellent performance was attributed to the stabilization of low-valent $Zn^{\delta+}$ species during CO_2RR as evidenced by time-dependent Raman and *operando* XAS measurements. Raman spectroscopy showed the presence of Zn–O bonds even after prolonged (300 min) electrolysis at 400 mA cm^{-2} current density. LCA of the XANES spectra revealed that 22% of the catalyst remained in an oxidized state after 35 minutes of CO_2RR, but these measurements were performed only at 50 mA cm^{-2}.[123]

The element-specificity and sensitivity to the local structure around the absorbing atom make XAS excellently suited for the investigation of metal–nitrogen doped carbon (M–N–C) catalysts, a promising family of single atom catalysts for CO_2RR.[7,54] The disordered nature and heterogeneity of these materials, and the sample-averaging nature of XAS, however, pose significant challenges in data analysis.[12] Ni–N–C materials were found to be excellent catalysts for CO production, but their long-term stability is a major issue, particularly at high current densities.[18,68,121] This might be overcome by understanding the

evolution of the active metal sites during operation. A catalyst containing dinuclear Ni_2 sites anchored on a N–C matrix exhibited 94.3% FE towards CO at 150 mA cm^{-2} current density in a microfluidic flow cell. *Operando* XAS measurements together with *ex situ* characterization revealed the presence of $Ni–N_4$ moieties with D_{4h} symmetry under open circuit conditions and a decrease in the Ni oxidation state with the application of reducing potentials. The Ni–N and Ni–Ni coordination numbers by EXAFS curve fitting in the as-prepared state were found to be 4.3 and 1.2, respectively. From this, the authors suggested the presence of a $Ni_2–N_6$ configuration, in which two $Ni–N_4$ units are connected through bridge N-atoms. In the electrolyte (without polarization), these Ni_2N_6 motifs adsorbed oxygen containing species, and formed an $O–Ni_2–N_6$ configuration with decreased Ni–Ni distance having an oxygen bridge between the two Ni atoms. The application of a reducing potential resulted in further shortening of the Ni–Ni distance, indicating that the presence of dinuclear Ni sites is the key for the CO_2RR activity.[121] NiS nanoparticles were found to outperform a Ni–N–C catalyst in terms of FE_{CO} at current densities above 300 mA cm^{-2} in a zero-gap electrolyzer, recently.[18] This was the first demonstration that a bulk Ni-compound exhibited high activity for CO production. To explain the origin of this intriguing selectivity, *operando* XAS analysis was performed. The high FE_{CO} for NiS was related to its similar local structure to that of Ni–N–C. According to the EXAFS analysis, the structure of the NiS electrode could be characterized by a distorted O_h symmetry with O_xS_y ligands. During CO_2RR, this structure lost oxygen, and a distorted D_{4h} symmetry was formed (Jahn-Teller effect), similar to the geometry of the $Ni–N_4$ motifs in Ni–N–C. Prolonged electrolysis in alkaline media, however, led to the loss of S species and the formation of Ni-hydroxide (evidenced by XPS), and thus the mimicked electronic structure disappeared. This resulted in loss of CO_2RR activity after 2 hours.[18]

Raman spectroscopy

Raman spectroscopy is an effective tool to study the chemical composition and structure of metal/metal oxide catalysts, as well as adsorbed intermediates and near-surface species during CO_2RR.[15,134] Surface-enhanced Raman spectroscopy (SERS) benefits from the enhancement of the Raman signal on certain metals (Ag, Au, Cu) and nanostructured electrodes, greatly improving the sensitivity and specificity of the technique.[134] It has been widely applied to identify active sites and to detect changes in the oxidation state of catalysts during reactions.[15] The possibility of detecting reaction intermediates, like *CO or *CHO, makes its use very important in mechanistic studies[85] and in the investigation of the effect of reaction conditions (*e.g.*, electrolyte effects). Furthermore, local pH measurements can also be performed, by detecting the near-surface ratio of buffer components, such as CO_3^{2-}/HCO_3^- or $H_2PO_4^{2-}/HPO_4^{2-}/PO_4^{3-}$[14]. One major advantage, compared to the complementary IR-spectroscopy, is the weak Raman scattering of water because of which measurements in aqueous electrolytes can be easily performed, which is very relevant for CO_2RR studies. This allows for a larger flexibility of cell designs and makes it suitable for the investigation for gas diffusion electrodes too.[51–53] Despite all these advantages, only a few works applied *operando* Raman spectroscopy under practically relevant conditions.[51–53,124,125] The relatively fixed design of flow CO_2 electrolyzers (*e.g.*, anode and cathode strictly facing each other, membrane separation, carbon-based GDEs or porous frits as catalyst supports) limits the achievable cell designs for performing *operando* Raman spectroscopy on a full-cell device. To the best of our knowledge only two works attempted to use Raman-spectroscopy in full electrolyzers (Fig. 8), to measure the local pH.[51,53] For the study of the catalyst surface structure and adsorbed intermediates, spectroelectrochemical flow cells, able to host GDEs (Fig. 7(A)), were reported, although in this configuration the operating conditions can be different from that of a practical device.[52,124,125]

In one of these works, the potential-dependent structural evolution of the catalyst and the presence of surface adsorbed intermediates were studied on bare Cu, CuAg and CuSn alloys.[125] Interestingly, the Cu_2O-related peaks persisted during CO_2RR at potentials down to −0.8 V *vs.* RHE (Fig. 7(B)), despite the thermodynamically favorable reduction to Cu under the given pH–potential conditions. The authors revealed that the intensity ratio of the peak related to the *CO stretching and the T_{2g} mode of Cu_2O showed very similar potential-dependence to the faradaic efficiency of CO. The highest ratio was found for the CuSn sample, correlating with its highest CO-selectivity. Overall, the results indicated that Cu_2O was formed in the reaction of Cu with hydroxide ions (byproduct of CO_2 reduction), but at higher concentration its presence blocked the active sites. Alloying Cu with Sn helped to reduce the passivating Cu_2O layer to the zero-valent state, resulting in increased density of active sites. The higher CO availability on the CuSn catalyst surface also led to higher FE for C_{2+} products. The same group also studied polymer-incorporated Cu electrodes by *operando* Raman spectroscopy in a GDE-setup.[124] The presence of polymers on the Cu surface altered the surface reactivity, and the degree of methylation of the polymers correlated with the CO_2RR activity/selectivity. With an amine-rich polymer, 87% FE for ethylene was achieved in a highly alkaline medium (10 M KOH). On this electrode, *operando* Raman spectroscopy

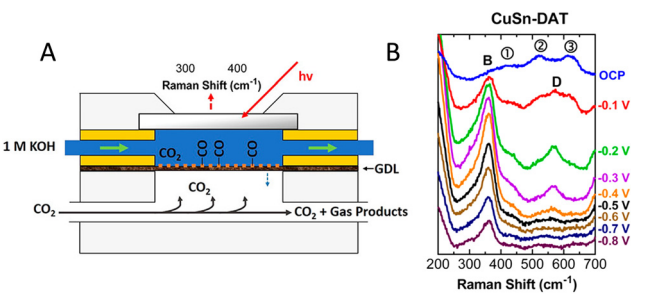

Fig. 7 (A) Schematic and photograph of a Raman spectroelectrochemical flow cell hosting a gas diffusion electrode. The cell mimics the conditions of a microfluidic CO_2 electrolyzer. (B) *Operando* SERS of a CuSn electrode during CO_2RR measured in the cell. Peak B is assigned to the frustrated rotational mode of adsorbed CO on Cu. Peaks D and 1, 2, 3 are SnO_2- and Cu_2O-related bands. Reproduced from ref. 125. Copyright 2019 ACS.

revealed the presence of an adsorbed CO (*CO) intermediate at a cathode potential of −0.47 V (*vs.* RHE), which could not be detected on the bare Cu and when a polymer with a high level of methylation was used. The latter catalysts showed significantly decreased ethylene (and overall CO_2RR) selectivity. The presence of amino groups, thus, seemed to help the accumulation of *CO, thereby assisting C–C coupling. Peaks assigned to adsorbed carboxylate ($*CO_2^-$) were also clearly observed on the polyamine modified Cu, indicating enhanced stabilization of intermediates by the amine groups.

Beyond the characterization of catalyst structure and surface intermediates, the application of Raman spectroscopy to measure local pH is also becoming more and more common. The same spectroelectrochemical Raman cell as in ref. 125 was used to study the potential dependence of the local pH on a Cu GDE in contact with different electrolytes.[52] The surface enhancement effect enabled to probe the local pH within 3 nm from the electrode surface (Fig. 2(D)). In a 1 M KOH electrolyte, the surface pH decreased from *ca.* 10 to 9.3 when the potential changed from −0.4 V to −1.3 V (*vs.* NHE). In parallel to this, peaks associated with basic copper carbonate (malachite) appeared, which showed similar potential dependence to the HCO_3^- peak. The authors explained this by the reaction of soluble Cu^{2+} species (originating from the initial reduction of CuO) with OH^- and CO_3^{2-} to form malachite. The consumption of the latter species resulted in a drop in the local pH (almost 5 pH unit difference compared to the bulk). At CO_2RR potentials (<−1.2 V *vs.* NHE) or at longer timescales, the pH started to increase, because of the completion of the oxide reduction, thus depletion of soluble Cu^{2+}, ceasing the malachite formation. The work highlighted that certain oxidized phases (*i.e.*, malachite), which are thermodynamically not stable under the given potential–pH conditions, can still persist, presumably because of their sluggish reduction kinetics. The presence of these species, in turn, can steer the CO_2RR selectivity.

Modified CO_2 electrolyzer designs (full cells) were also reported that allow for local pH-measurements near the cathode (Fig. 8(A) and (B)). In one work, the pH gradient in the catholyte layer of a membrane-separated microfluidic cell (Fig. 8(A)) was measured in a distance of 40–120 μm from the cathode and extrapolated to the electrode surface.[53] The modified flow cell was 3D-printed from a photosensitive resin and a plastic film cover was placed on the top of the cell to allow transparency for the beam. The Raman beam was parallel to the GDE and was moved in the perpendicular (x) direction towards the bulk of the electrolyte to measure the pH gradient. Without polarization in a 1 M KOH electrolyte, the pH at the electrode surface was 7.2, much lower than the bulk value, because of the neutralization reaction between OH^- and CO_2. Moving away from the electrode surface to the bulk electrolyte, the pH increased to above 11 at a distance of 120 μm. When applying 50 mA cm^{-2} current density to the cell (Fig. 8(C)), the pH increased at the electrode surface to *ca.* 9, because of the production of OH^- during CO_2RR. In this case, the region where HCO_3^- could be detected (*i.e.*, pH < 11) was 40 μm narrower than at open circuit potential (OCP). With increasing current density, the HCO_3^- region shrank further and the cathode surface pH gradually increased (>12 at 150 mA cm^{-2}). These results showed that the produced OH^- during CO_2RR cannot fully offset the OH^- consumed by the reaction with CO_2 and the usually observed nominal overpotential-reduction in alkaline electrolytes was attributed to the buildup of a Nernst potential at the cathode/electrolyte interface.[53]

Local pH measurement in a zero-gap bicarbonate electrolyzer with a bipolar membrane (Fig. 8(B)) was also demonstrated.[51] In this cell design the laser beam was perpendicular to the silver-foam cathode, which was illuminated through a sapphire window

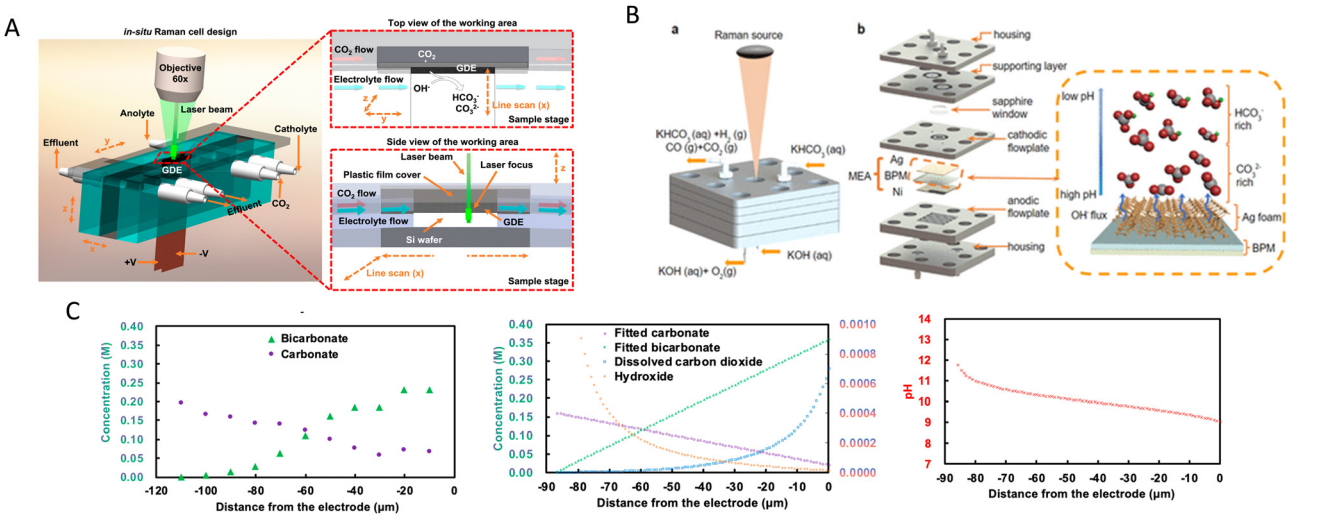

Fig. 8 (A) Microfluidic flow cell designed for local pH measurements. Reproduced from ref. 53. Copyright 2020 ACS. (B) Bipolar membrane-bicarbonate electrolyzer for local pH measurements. Reproduced from ref. 51. Copyright 2020 ACS. (C) Measurement of local pH with Raman spectroscopy in the *operando* cell shown in panel C using a 1 M KOH electrolyte at 50 mA cm^{-2} current density. Measured HCO_3^- and CO_3^{2-} concentrations as a function of distance from the electrode surface, fitted concentrations of dissolved species and the derived pH values. Reproduced from ref. 53. Copyright 2020 ACS.

placed in the center of the cathodic flow plate. The use of a silver foam cathode was necessary to eliminate the carbon based GDLs which would obscure the electrocatalyst and the strong Raman signal of carbon would hinder the detection of HCO_3^- and CO_3^{2-}. The cell modification, however, resulted in the deterioration of the performance (32% FE for CO at −1.3 V *vs.* Ag/AgCl). The surface pH increased during the reduction of bicarbonate, which became more prominent as the current density increased. When applying 200 mA cm^{-2} current density, the surface pH changed from 8.53 (OCP) to 10.31 after 5 minutes of electrolysis. A pH gradient established in this electrolyzer too: at 200 mA cm^{-2} the pH was around 1.3 units lower at a distance of 150 μm from the electrode, compared to the catalyst surface. Higher current densities led to thicker diffusion layers, explained by the production of OH^- during bicarbonate electrolysis, which prevailed over the bubble-induced convection, transporting OH^- away from the electrode surface. When increasing the temperature of the bicarbonate solution feed from 20 °C to 70 °C, the surface pH slightly increased (with 0.6 pH units) and the FE for H_2 production dropped from 32% to 15% (at 50 mA cm^{-2} total current density). These results indicated that a higher surface pH diminishes HER in bicarbonate electrolyzers (in contrast to alkaline water electrolysis).

Ratiometric techniques for local pH measurements

Besides Raman spectroscopy, ratiometric techniques were also employed for local pH measurements. A pH-sensitive ratiometric probe (dye) has two or more absorption/emission bands that respond differently to the proton concentration.[30] Within a certain pH-range, the ratio of the intensity of the absorption peaks at different wavelengths is directly correlated with the pH. Confocal fluorescent microscopy with micron-scale resolution in the *x*, *y*, *z* direction[50] has been used to probe the pH within trenches of a Cu GDE. A two-color pH-sensitive fluorescent dye was added to the electrolyte ($KHCO_3$). With increasing current density (up to 28 mA cm^{-2}), the local pH increased both at the GDE surface and within the trenches (as expected), but spatial inhomogeneity was observed. As OH^- ions are produced in both CO_2RR and HER, the higher local pH was used as an indication for higher activity regions. When the average pH at the surface of the electrode was below 9.5, the electrode mostly produced C_1 products and H_2, while many C_2 products were observed at pH values above 10. Randomly distributed trenches with an average width of (18 ± 8) μm were present in the microporous layer of the GDE. Interestingly, higher pH was observed within the narrow trenches indicating higher local activity in more confined regions of the GDE.

A clever method to manipulate and measure the local pH in MEAs was recently demonstrated.[30] The authors aimed to tune the local pH in a bipolar membrane electrolyzer at the catalyst/CEM interface to diminish acidity, and thus increase CO_2RR selectivity. The local chemical environment of a BPM (consisting of a Nafion CEL and a graphene-oxide-based AEL) was modified by a weak-acidic polyelectrolyte consisting of poly(acrylic-acid) and poly(allylamine hydrochloride) (PAA–PAH) bilayers. Ratiometric dyes were covalently attached to the amine groups of PAH, allowing for *in situ* pH measurements at different distances from the cathode/CEL interface, depending on the number of PAH/PAA buffer layers between the dye and the Nafion. The local pH was quantified by UV-Vis spectroscopy. Without polarization, with the increasing number of PAA/PAH buffer layers, the pH gradually increased from *ca.* 3 to > 6. When applying a 4 mA cm^{-2} reverse bias, the pH in layers close to the Nafion decreased, because more protons were introduced into the CEL. In layers further away from the Nafion, the proton concentration, however, did not change significantly. This suggested that the pH changes occur within a much shorter distance in weak-acidic CEMs (50 nm), compared to typical boundary layer thicknesses at the electrified solid/liquid interface (20–200 μm).

Scanning probe techniques

Scanning probe techniques are powerful tools to investigate the surface topography and local activity of electrocatalysts. In scanning electrochemical microscopy (SECM) a nanometer-sized tip electrode is positioned in close proximity to the electrode surface functioning as a local probe to determine reaction rates or local concentrations. Its applicability to study GDEs was recently demonstrated for both ORR[135] and CO_2RR.[136,137] A Pt microelectrode is suitable to detect OH^- and H_2O activities near the electrode, as the potential of PtO reduction depends on these parameters. With a shear-force based approach, a Pt microelectrode was positioned at 100 nm above a silver GDE.[137] When applying increasingly negative potentials to the silver cathode, the PtO reduction potential shifted gradually towards more negative potentials. At the highest applied potential (−1.69 V *vs.* Ag/AgCl, ~12 mA cm^{-2}) the measured hydroxide/water activity ratio was beyond that was obtained for a 16 M KOH solution, indicating a highly alkaline environment near and inside the GDE.[137] SECM was also used to investigate the effect of catalyst loading and CO_2 back pressure on the activity (local CO product fluxes) of a gold GDE (Fig. 9(A)).[136] Using a shear-force based approach, the CO formation rate was detected by measuring diffusion limited CO oxidation current on the Au nanoelectrode (tip) positioned at a sub-μm distance from the Au GDE. For a GDE with a shallow loading-gradient, the increase in catalyst loading led to a nearly linear increase in the amount of produced CO. Regions with increased activity (5–6 times higher currents) were also identified. At these hotspots, the CO-current was of similar magnitude or even higher at the low-loading areas, compared to those with high loading. This indicated that at low catalyst loading the formation of a three-phase boundary is more important to reach high activity, than the amount of catalyst. For the GDE with a steeper loading gradient, the activity decreased at the higher loading areas (Fig. 9(A)), because part of the catalyst nanoparticles were not accessible to the CO_2. Recording the topography profile of the GDE showed that lower *Z*-positions (*e.g.*, above a pore) coincided with higher CO-formation activity. A high-resolution activity map was also recorded within an area of similar loading. Surprisingly, large activity differences were found, indicating that inhomogeneous pore distribution significantly impacts local activity. The study also revealed that at lower CO_2 back pressures, a large amount of catalyst remains unutilized, as the CO_2 cannot reach

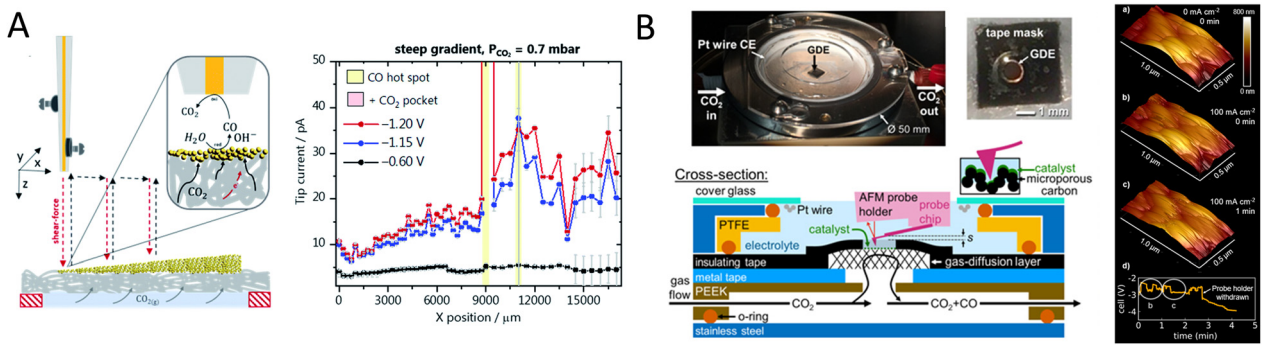

Fig. 9 Scanning probe methods applied to study CO_2RR in GDE-configurations. (A) SECM experimental setup operated in a surface-generation tip-collection mode to measure local CO_2RR activity on a Au-GDE with varying loadings (left). SECM array scans along the catalyst loading-gradient at different potentials applied to the GDE (right). The tip current is proportional to the CO production rate. Reproduced from ref. 136. Copyright 2019 the Authors, Published by RSC. (B) Schematic and photos of an EC-AFM cell (left). EC-AFM images of a Cu-sputtered GDE at 100 mA cm^{-2} (right). Reproduced from ref. 126. Copyright 2021 the Electrochemical Society. Reproduced by permission of IOP Publishing. All rights reserved.

the upper catalyst layers. Consequently, higher catalyst loading only leads to higher activity for CO_2RR, when enough CO_2 is supplied, and properties of the GDLs (hydrophobicity, pore structure, permeability) will have a significant impact on the optimal loading-CO_2 back pressure combinations.[136]

Electrochemical atomic force microscopy (EC-AFM) can provide *operando* topography and spatial maps of mechanical properties (*e.g.*, adhesion, deformation), as well as insights into changes in catalyst surface faceting, agglomeration or degradation.[126,138,139] While EC-AFM was previously limited to low current densities, because of bubble formation disturbing measurements, a suitable cell design hosting a GDE, and allowing for gas products to leave through the diffusion media, can enable high current density EC-AFM measurements.[126] A commercial EC-AFM cell was modified to allow for gas flow below the GDE, with a stagnant electrolyte on the catalyst side (Fig. 9(B)), and its applicability was demonstrated at high current densities up to 100 mA cm^{-2}. Technical challenges related to bubble formation, mechanical stability of the cell and trade-off between temporal resolution and scan size have been discussed. The reported cell allowed for the observation of morphological restructuring of catalysts, as well as carbonate precipitate formation. The investigated Cu films had very stable topography and mechanical property maps with no signs of restructuring or precipitate formation. Because of the small scan size, however, certain areas could remain hidden; therefore the technique needs to be further improved to increase the scan size. At higher current densities, electrolyte flooding also impeded long-term measurements (<3 min at 100 mA cm^{-2}).

Mass spectrometry

Mass spectrometry offers real-time product detection, which is extremely important to capture rapid changes in the product distribution, for instance, during initial periods of catalysis and for dynamically changing systems (*e.g.*, pulsed CO_2RR). Furthermore, the detection of (unstable) reaction intermediates, present even in very small amounts close to the catalyst surface, can also largely contribute to our understanding of the reaction mechanism. In this regard, isotopic labeling is also of particular importance.[47] Considering this fact, differential electrochemical mass spectrometry (DEMS) and online electrochemical mass spectrometry (OLEMS) became powerful tools for the real time detection of CO_2/CO reduction products,[109,140] despite some general limitations such as their inability to detect non-volatile species and the convolution of CO_2 and CO signals.[141,142] Notwithstanding the high mechanistic information content of electrochemical mass spectrometry (EC-MS) studies, interestingly, only few studies exist so far which took advantage of flow cells or GDE-configurations.[81,127] A flow electrolyzer mass spectrometry (FEMS) technique combined with isotopic labeling was recently applied to study the origin of oxygen in CO/CO_2RR intermediates (acetaldehyde) and products (ethanol, *n*-propanol).[27] A membrane-less microfluidic cell with a flowing KOH electrolyte, and having a capillary probe for the MS placed in close proximity of the Cu GDE, was used for these studies (Fig. 10). The high current density (150 mA cm^{-2}) obtained with the GDE setup allowed the detection of reactive species present in very low concentrations, which would be below the detection limit in an H-cell. By following *m*/*z* values relevant for *n*-propanol, acetaldehyde and ethanol, and using unlabeled and ^{18}O-labeled CO and electrolyte ($H_2{}^{18}O$) feeds, the authors found that while the O of acetaldehyde originated from CO, that of ethanol largely came from the electrolyte. This finding could be rationalized by a mechanism, in which the formed acetaldehyde goes through a rapid O-exchange with water, and then is further reduced to ethanol (Fig. 10(B)). The cross-coupling of acetaldehyde with CO, however, was found to be an unlikely route for the formation of C_3 products. A gas accessible membrane electrode (GAME) system is composed of a cylindrical gas compartment with a porous polycarbonate-based GDE at the end, together placed in a stagnant electrolyte.[140] In this configuration a GDE-interface is created, however, with a much thinner substrate (12 µm) compared to typical carbon-based GDEs (~250 µm). This further enhances reactant and product transport, facilitating real-time detection of products with mass spectrometry. The electrocatalytic reaction sites and gas-sampling interface are collocated, and therefore the delay time for MS analysis is minimized. At the same time, an ultramicroelectrode (UME) can be positioned in proximity of the catalyst in the electrolyte for liquid product analysis or local pH

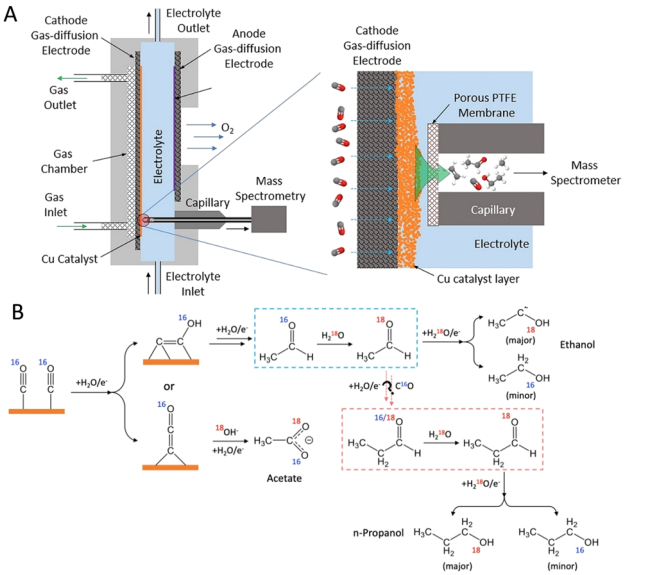

Fig. 10 (A) Schematic of the flow electrolyzer-mass spectrometry (FEMS) setup. (B) Proposed reaction mechanism for CO reduction to oxygenated products. Reproduced from ref. 81. Copyright Wiley-VCH GmbH.

measurements. With this setup the formation of H_2, CH_4 and C_2H_4 on a Cu–Au electrode was simultaneously detected with time resolution good enough to deconvolute the faradaic current during a cyclic voltammetry scan with 1 mV s^{-1} scan rate to the partial current of products. A Pt UME was also placed close (<100 μm) to the catalyst, and the voltammetric response of PtO reduction was used as a sensor for the local pH variation.

Besides detecting products and reaction intermediates, EC-MS methods could also be used to measure local CO_2 concentrations near the catalyst surface. A DEMS method was reported to directly observe the local reaction environment during CO_2RR in a custom-designed cell with dissolved CO_2 as the reactant. The catalyst was directly deposited on the pervaporation membrane at the interface between the electrochemical cell and the mass spectrometer.[141] By this approach the authors could experimentally observe the reaction between CO_2 and the cathodically formed OH^- and its influence on CO_2RR. Such measurements would be extremely relevant for GDE-based continuous flow electrolyzers too, as the local CO_2 concentration directly affects the CO_2RR rate and the product distribution as well.

Neutron and X-ray imaging

Neutron- and X-ray radiography are non-destructive imaging techniques allowing *in situ*/*operando* characterization of processes taking place in energy devices, such as fuel cells, batteries or electrolyzers.[143–145] The different interactions of neutrons and X-rays with matter make the two techniques largely complementary in materials science.[144,146] Neutron radiography can give strong contrast for some elements located close to each other in the periodic table and is able to differentiate between isotopes as well (*e.g.*, ^1H and ^2D).[146] Neutrons penetrate, however, easily into materials composed of heavy elements (metals) which are typically used for the cell body of electrochemical devices. This makes neutron imaging excellently suited for *in situ*/*operando* investigations without the need for major cell modifications. In contrast, as X-rays interact with electrons of the atom, their attenuation increases with the increase in the atomic number of the element. Therefore, for X-ray imaging usually an X-ray window has to be placed in the cell to enable the beam to reach the core of the device. Synchrotron X-ray radiography has better spatial resolution (1 μm) than neutron imaging with short exposure times, however at the expense of reduced field of view.[147] Both techniques have been widely used to characterize the water management in fuel cells or water electrolyzers.[148–150] As usually gas-phase reactants and/or products are present in these devices, the observation of gas bubbles and their distribution within the cell is also crucial to study the two-phase transport phenomena,[151] which can be performed with both neutron and X-ray radiography. Tomography (*i.e.*, 3D spatially resolved imaging) is also feasible with both techniques, resulting in detailed characterization of the microstructure of the entire cell.[150,152] The X-ray and neutron radiographic characterization of CO_2 electrolyzers is still in its infancy, as we can find only a few reports on such studies. These are focused on the membrane hydration, water distribution across the MEA and gas bubble formation in the electrolyte layers.[78,91,100,128,129]

To maintain a high ionic conductance, therefore fast ion transport in CO_2 electrolyzers, it is necessary for the ion exchange membrane to be in a well-hydrated state.[31] Recently neutron imaging was employed to directly quantify liquid water distribution across a MEA (Fig. 11(A)).[91] Increasing the relative humidity (0–100%) of the reactant CO_2 resulted in lower cell voltage, which stemmed from reduced ohmic losses, when a humidified reactant was used. To explain the origin of this observation, the through-plane (perpendicular to the flow-field) water-content of the MEA was characterized. The increase in the relative humidity resulted in a *ca.* 60% increase in the liquid water volume of the Nafion membrane at 575 mA cm^{-2} current density. The membrane, however, also experienced a gradual dehydration during operation when increasing the current density, which resulted in decreased ionic conductivity. The dehydration was most significant at the center, compared to the regions in contact with the anode and cathode catalysts (Fig. 11(A)). While this study gave interesting insights into the water transport by directly measuring the water uptake of the membrane, the cell significantly underperformed state-of-the art CO_2 electrolyzers, possibly because of the modified cell design optimized for the neutron imaging experiment and the acidic local environment at the catalyst–CEM interface.

The same group also employed high spatial resolution (15 μm) neutron imaging to study the formation of gas bubbles in the catholyte layer of a CO_2 electrolyzer, which they correlated to performance instability.[128] The gas saturation of a 3 M $KHCO_3$ electrolyte increased with increasing current density to 50 mA cm^{-2}, then it reached a plateau. The dispersion in the cathode potential was correlated to the gas saturation of the electrolyte. In the lower current density region, a strong positive correlation was found between the two parameters (semi-stable operation),

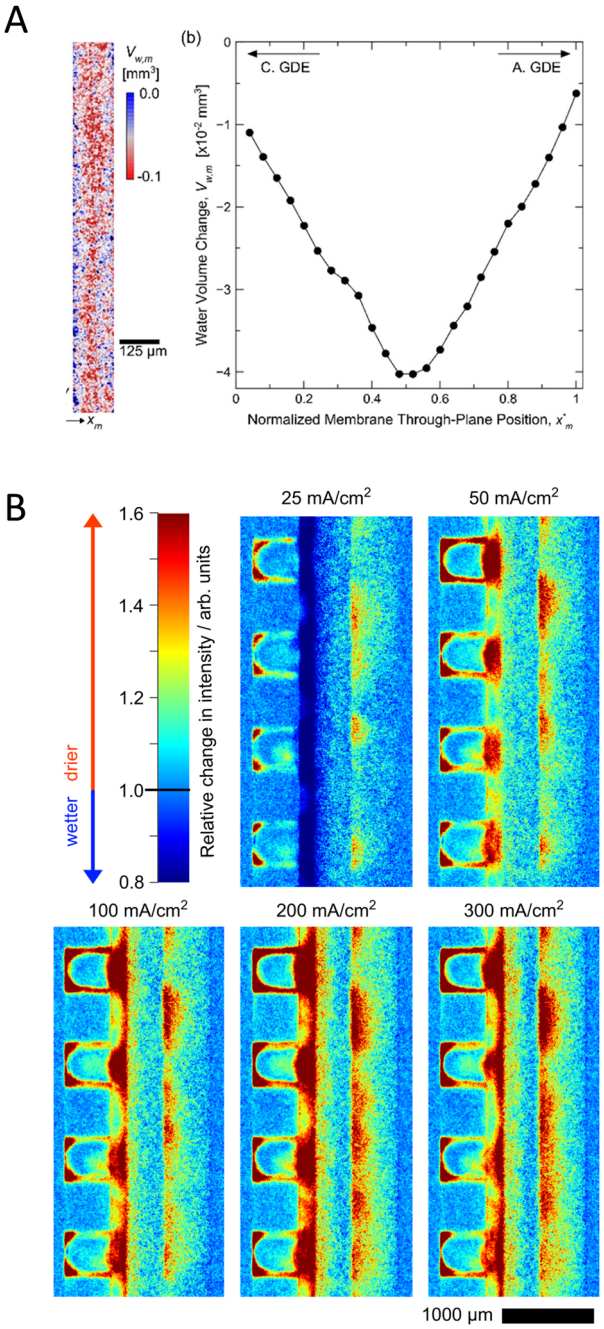

Fig. 11 *Operando* visualisation and quantification of water management in CO_2 electrolyzers. (A) Quantification of liquid water content in a MEA by neutron radiography. Processed image highlighting the water volume change in the CEM. Water-volume change across the membrane is plotted on the graph. Reproduced from ref. 91. Copyright 2020 ACS. (B) Relative change in the water-content of a zero-gap CO_2 electrolyzer during operation. Reproduced from ref. 100. Copyright the Authors, published by Springer Nature.

indicating that the unstable cathode potential was the result of gas accumulation in the electrolyte layer. At higher current densities, the number of gas removal pathways increased to maintain a constant electrolyte gas saturation. In this region the increased rate of transient gas accumulation (production) and its removal altered mass transport in the cell, and caused an increased cathode potential instability. The authors suggested that keeping the gas saturation below the plateau (oscillation) region would result in increased performance stability; therefore it is critical to improve gas management in CO_2 electrolyzers. High resolution neutron imaging (6 µm) was also performed in a zero-gap AEM electrolyzer (with Ag catalyst) to study water distribution and to observe salt precipitation at the cathode.[100] Up to 200 mA cm^{-2} the cathode became gradually dryer with increasing current density, because of the increased water consumption and electroosmotic drag from the cathode to the anode (Fig. 11(B)). At 300 mA cm^{-2}, however, in some regions of the cathode the radiographic intensity even decreased. This counter-intuitive observation was explained by the accumulation of $KHCO_3$ salts, which were preferably located in the channel *vs.* land area of the flow field. Although salt accumulation already started at 100 mA cm^{-2} current density, at this lower current gas transport was still sufficient to maintain high CO selectivity. A more pronounced bubble accumulation on the anode side in the region of the cathode land was also observed, suggesting higher local reaction rates in the cathode land region. This work nicely demonstrated the potential of neutron imaging to investigate water transport and salt precipitation in AEM-based CO_2 electrolyzers, which might contribute to mitigate the carbonate problem in the future.

Synchrotron X-ray radiography was used to study the effect of operating temperature on the membrane hydration and gas/water content in a CEM zero-gap CO_2 electrolyzer.[78] The cell voltage and thus the overall power density reduced by *ca.* 35% when raising the temperature from 25 to 60 °C, as a result of the simultaneous reduction of activation, ohmic and mass transport losses. The radiographic images of the CEM at higher temperatures indicated higher water content, resulting in increased ionic conductivity and thus decreased ohmic losses. To study the anodic and cathodic mass transport limitations, the impact of temperature on gas saturation in the anode and cathode GDEs was also investigated. The authors found that mass transport losses increased with increasing current density. A modular cell for X-ray radiographic imaging of electrolyte distribution in strongly absorbing Ag GDEs was reported recently.[129] Electrolyte intrusion into and distribution within the GDE were observed for ORR and CO_2RR. For the CO_2RR studies, a cell with AEM-separated anolyte and catholyte chambers was employed. To allow for the irradiation, an X-ray window was cut in the middle of the cell, and the cell was irradiated from the anode side. 300 mA cm^{-2} steady-state current density was reached at −1.0 V (*vs.* RHE) cathode potential; however, no selectivity data were reported. At lower potentials (−0.7 V), larger pore systems got filled up with the electrolyte, while at more negative potentials (−1.0 V *vs.* RHE) electrolyte droplets and gas bubbles also appeared on the gas and electrolyte side, respectively. On a more hydrophobic catalyst (higher PTFE-content) gas formation was already observed at −0.7 V, which became even more prominent at −1.0 V. Furthermore, electrolyte distribution was strongly retarded on this GDE, compared to the catalyst with lower PTFE-content. Formation of salt crystallites was observed at −0.7 V, which were washed

away at −1.0 V, because of the intensified flooding at this potential.

As highlighted above, radiography has potential in the *operando* investigation of CO_2 electrolyzers, in particular to identify the origin of overvoltages (*e.g.*, membrane hydration) and cell failure mechanisms (*e.g.*, precipitate formation, flooding, *etc.*). Neutron- and X-ray radiography are, however, expensive techniques as synchrotron or neutron facilities are required. Because of this, visual observation of the inner part of the cell by high-speed cameras is also very appealing to observe flooding or salt precipitation under laboratory conditions. In one work, the observation of precipitate formation was combined with the measurement of relative humidity (RH) and temperature by embedded sensors to characterize and model water transport within an AEM-separated zero-gap cell.[73] The relative humidity was measured before and during CO_2RR (at 100 mA cm^{-2}) at different locations within the cell with dry (0% RH) and wet (70% RH) CO_2 feeds. While the wet CO_2 feed evenly humidified the cathode flow field, large spatial differences were observed when a dry feed was applied. It was shown that the operating parameters can be varied to adjust water transport across the membrane. The increased membrane transport may enhance cation crossover from the anolyte,[22] resulting in detrimental precipitate formation at the cathode, but also promoting CO_2RR. To visually observe this together with cathode flooding, a transparent window was incorporated into the cell. For the dry CO_2 feed at 100 mA cm^{-2}, liquid formation in the flow field could be observed after 20 minutes and salt precipitation after 120 minutes. The use of a wet CO_2 feed, however, prolonged the salt and liquid accumulation to >150 mA cm^{-2}, in accordance with the lower flux of water across the membrane.

Thermography

As with the increase of cell size or number of cell stacks, higher spatial variation in operating conditions is expected, probing local activities in a full electrolyzer device can assist scale-up efforts. Recently, location-specific catalytic activity was studied by infrared thermography,[130] making use of the inefficient charge transfer and transport, resulting in heat generation. The authors postulated that any temperature change of the catalyst was primarily because of heat generation from the electrochemical reaction at the cathode. Therefore, observing the temperature change during operation can be a measure of electrochemical activity. For instance, a higher temperature increase was observed for Pt than Ag during HER at a fixed potential, in accordance with their known activity trend towards HER. Spatial mapping can also provide a means to examine transport phenomena or limiting chemical reactions, as uneven current distribution (thus temperature) can be the result of poor catalyst deposition, different aging of catalyst portions or spatially varying operating conditions. The influence of electrolyte flow on the reaction rate distribution was studied by changing the direction of the electrolyte flow from ''bottom to top'' to ''side to side''. In the latter case, gas bubbles (O_2) become trapped in the anode compartment, resulting in noisy LSV curves and rapidly changing temperature profiles of the cathode GDE. This was rationalized by shielding the Ni mesh anode by the buildup of gas, resulting in uneven current density distribution. As the reaction of CO_2 with hydroxide ions is highly exothermic, carbonate formation can also be followed by thermography during CO_2RR as demonstrated by a larger temperature increase when changing the gas feed from N_2 to CO_2.

Conclusions and future prospects

As highlighted in this Feature Article, there is a tendency in the CO_2RR research field to implement *operando* techniques in full electrolyzer devices or in GDE-setups to gain mechanistic understanding of the processes taking place under practically relevant conditions. The transition from low to high current density *operando* characterization, however, started only very recently, in the past 2–3 years. Consequently, there is still a large undiscovered research space, which has to be explored in the near future. Previous studies demonstrated the potential of *operando* characterization to serve as a tool to uncover the catalyst microenvironment, optimize working conditions, understand reaction mechanisms, or to identify reasons for device failure. Nevertheless, in several cases the *operando* techniques were applied to underperforming devices or without reporting activity/selectivity data. To make these measurements more representative of the real working environment, more intensive collaboration among electrochemists, spectroscopists and cell development engineers is needed to overcome technical challenges and maximize electrolyzer performance and spectroscopic data quality at the same time.

Combination of different *operando* methods and their coupling to real-time product analysis would provide invaluable structure–performance correlations, helping to understand and deconvolute the multitude of processes taking place in a CO_2 electrolyzer. As the CO_2RR current densities have already reached industrially relevant values, the field should focus on improving energy-efficiency and durability of the electrolyzers. *Operando* methods can largely assist and accelerate the identification of the origin of voltage losses and cell deactivation mechanisms. In particular radiographic imaging will be an excellent tool for this when combined with elemental analysis. The selective production of high-value multicarbon products will largely benefit from the understanding of the C–C coupling mechanism at high current densities. Catalyst degradation studies, for instance by on-line ICP-MS,[70,153] should also be performed in GDE-configurations in the future. Finally, more focus should be put on electrolyte-engineering, which was shown to be very efficient to tune selectivity and increase activity in H-type cells, but is only marginally researched in continuous-flow CO_2RR.

Conflicts of interest

There are no conflicts to declare.

Acknowledgements

This project has received funding under the European Union's Horizon Europe research and innovation program from the European Research Council (ERC, Grant Agreement No. 101043617) and the FlowPhotoChem project (grant agreement ID: 862453). We also thank the Hungarian Renewable Energy National Laboratory for support, financed by the RRF-2.3.1-21-2022-00009 project.

Notes and references

1 P. De Luna, C. Hahn, D. Higgins, S. A. Jaffer, T. F. Jaramillo and E. H. Sargent, *Science*, 2019, **364**, eaav3506.
2 A. A. Samu, A. Kormányos, E. Kecsenovity, N. Szilágyi, B. Endrődi and C. Janáky, *ACS Energy Lett.*, 2022, **7**, 1859–1861.
3 Y. Hori, H. Wakebe, T. Tsukamoto and O. Koga, *Electrochim. Acta*, 1994, **39**, 1833–1839.
4 H. Mistry, A. S. Varela, C. S. Bonifacio, I. Zegkinoglou, I. Sinev, Y.-W. Choi, K. Kisslinger, E. A. Stach, J. C. Yang, P. Strasser and B. R. Cuenya, *Nat. Commun.*, 2016, **7**, 12123.
5 A. Herzog, A. Bergmann, H. S. Jeon, J. Timoshenko, S. Kühl, C. Rettenmaier, M. Lopez Luna, F. T. Haase and B. Roldan Cuenya, *Angew. Chem., Int. Ed.*, 2021, **60**, 7426–7435.
6 A. M. Ismail, G. F. Samu, Á. Balog, E. Csapó and C. Janáky, *ACS Energy Lett.*, 2019, **4**, 48–53.
7 W. Ju, A. Bagger, G.-P. Hao, A. S. Varela, I. Sinev, V. Bon, B. Roldan Cuenya, S. Kaskel, J. Rossmeisl and P. Strasser, *Nat. Commun.*, 2017, **8**, 944.
8 D. Hursán, A. A. Samu, L. Janovák, K. Artyushkova, T. Asset, P. Atanassov and C. Janáky, *Joule*, 2019, **3**, 1719–1733.
9 G. Marcandalli, M. C. O. Monteiro, A. Goyal and M. T. M. Koper, *Acc. Chem. Res.*, 2022, **55**, 1900–1911.
10 X. Li, S. Wang, L. Li, Y. Sun and Y. Xie, *J. Am. Chem. Soc.*, 2020, **142**, 9567–9581.
11 J. Li and J. Gong, *Energy Environ. Sci.*, 2020, **13**, 3748–3779.
12 J. Timoshenko and B. Roldan Cuenya, *Chem. Rev.*, 2021, **121**, 882–961.
13 R. Kas, O. Ayemoba, N. J. Firet, J. Middelkoop, W. A. Smith and A. Cuesta, *ChemPhysChem*, 2019, **20**, 2904–2925.
14 M. C. O. Monteiro and M. T. M. Koper, *Curr. Opin. Electrochem.*, 2021, **25**, 100649.
15 H. Li, P. Wei, D. Gao and G. Wang, *Curr. Opin. Green Sustainable Chem.*, 2022, **34**, 100589.
16 B. Endrődi, G. Bencsik, F. Darvas, R. Jones, K. Rajeshwar and C. Janáky, *Prog. Energy Combust. Sci.*, 2017, **62**, 133.
17 G. L. De Gregorio, T. Burdyny, A. Loiudice, P. Iyengar, W. A. Smith and R. Buonsanti, *ACS Catal.*, 2020, **10**, 4854–4862.
18 M. H. Han, D. Kim, S. Kim, S.-H. Yu, D. H. Won, B. K. Min, K. H. Chae, W. H. Lee and H.-S. Oh, *Adv. Energy Mater.*, 2022, **12**, 2201843.
19 D. Higgins, C. Hahn, C. Xiang, T. F. Jaramillo and A. Z. Weber, *ACS Energy Lett.*, 2019, **4**, 317–324.
20 B. Endrődi, E. Kecsenovity, A. Samu, T. Halmágyi, S. Rojas-Carbonell, L. Wang, Y. Yan and C. Janáky, *Energy Environ. Sci.*, 2020, **13**, 4098–4105.
21 F. P. García de Arquer, C.-T. Dinh, A. Ozden, J. Wicks, C. McCallum, A. R. Kirmani, D.-H. Nam, C. Gabardo, A. Seifitokaldani, X. Wang, Y. C. Li, F. Li, J. Edwards, L. J. Richter, S. J. Thorpe, D. Sinton and E. H. Sargent, *Science*, 2020, **367**, 661–666.
22 B. Endrődi, A. Samu, E. Kecsenovity, T. Halmágyi, D. Sebők and C. Janáky, *Nat. Energy*, 2021, **6**, 439–448.
23 D. Reinisch, B. Schmid, N. Martić, R. Krause, H. Landes, M. Hanebuth, K. J. J. Mayrhofer and G. Schmid, *Zeitschrift für Physikalische Chemie*, 2020, **234**, 1115–1131.
24 T. Burdyny and W. A. Smith, *Energy Environ. Sci.*, 2019, **12**, 1442–1453.
25 A. S. Varela, M. Kroschel, T. Reier and P. Strasser, *Catal. Today*, 2016, **260**, 8–13.
26 H. Liu, H. B. Tao and B. Liu, *J. Phys. Chem. Lett.*, 2022, **13**, 6520–6531.
27 Á. Vass, A. Kormányos, Z. Kószó, B. Endrődi and C. Janáky, *ACS Catal.*, 2022, **12**, 1037–1051.
28 P. Kamat and P. Christopher, *ACS Energy Lett.*, 2022, **7**, 1469–1472.
29 C. Kim, J. C. Bui, X. Luo, J. K. Cooper, A. Kusoglu, A. Z. Weber and A. T. Bell, *Nat. Energy*, 2021, **6**, 1026–1034.
30 Z. Yan, J. L. Hitt, Z. Zeng, M. A. Hickner and T. E. Mallouk, *Nat. Chem.*, 2021, **13**, 33–40.
31 G. M. Geise, M. A. Hickner and B. E. Logan, *ACS Appl. Mater. Interfaces*, 2013, **5**, 10294–10301.
32 D. T. Whipple, E. C. Finke and P. J. A. Kenis, *Electrochem. Solid-State Lett.*, 2010, **13**, B109–B111.
33 S. Ma, M. Sadakiyo, R. Luo, M. Heima, M. Yamauchi and P. J. A. Kenis, *J. Power Sources*, 2016, **301**, 219–228.
34 T. Haas, R. Krause, R. Weber, M. Demler and G. Schmid, *Nat. Catal.*, 2018, **1**, 32–39.
35 J. J. Kaczur, H. Yang, Z. Liu, S. D. Sajjad and R. I. Masel, *Front. Chem.*, 2018, 6.
36 I. E. L. Stephens, K. Chan, A. Bagger, S. W. Boettcher, J. Bonin, E. Boutin, A. K. Buckley, R. Buonsanti, E. R. Cave, X. Chang, S. W. Chee, A. H. M. da Silva, P. de Luna, O. Einsle, B. Endrődi, M. Escudero-Escribano, J. V. Ferreira de Araujo, M. C. Figueiredo, C. Hahn, K. U. Hansen, S. Haussener, S. Hunegnaw, Z. Huo, Y. J. Hwang, C. Janáky, B. S. Jayathilake, F. Jiao, Z. P. Jovanov, P. Karimi, M. T. M. Koper, K. P. Kuhl, W. H. Lee, Z. Liang, X. Liu, S. Ma, M. Ma, H.-S. Oh, M. Robert, B. R. Cuenya, J. Rossmeisl, C. Roy, M. P. Ryan, E. H. Sargent, P. Sebastián-Pascual, B. Seger, L. Steier, P. Strasser, A. S. Varela, R. E. Vos, X. Wang, B. Xu, H. Yadegari and Y. Zhou, *J. Phys. Energy*, 2022, **4**, 42003.
37 J. M. Spurgeon and B. Kumar, *Energy Environ. Sci.*, 2018, **11**, 1536–1551.
38 M. Jouny, G. S. Hutchings and F. Jiao, *Nat. Catal.*, 2019, **2**, 1062–1070.
39 J. E. Huang, F. Li, A. Ozden, A. Sedighian Rasouli, F. P. García de Arquer, S. Liu, S. Zhang, M. Luo, X. Wang, Y. Lum, Y. Xu, K. Bertens, R. K. Miao, C.-T. Dinh, D. Sinton and E. H. Sargent, *Science*, 2021, **372**, 1074–1078.
40 W. Ma, S. Xie, T. Liu, Q. Fan, J. Ye, F. Sun, Z. Jiang, Q. Zhang, J. Cheng and Y. Wang, *Nat. Catal.*, 2020, **3**, 478–487.
41 C. Peng, S. Yang, G. Luo, S. Yan, M. Shakouri, J. Zhang, Y. Chen, W. Li, Z. Wang, T.-K. Sham and G. Zheng, *Adv. Mater.*, 2022, **34**, 2204476.
42 B. Kim, F. Hilman, M. Ariyoshi, S. Fujikawa and P. J. A. Kenis, *J. Power Sources*, 2016, **312**, 192–198.
43 N. T. Nesbitt, T. Burdyny, H. Simonson, D. Salvatore, D. Bohra, R. Kas and W. A. Smith, *ACS Catal.*, 2020, **10**, 14093–14106.
44 M. Dunwell, Q. Lu, J. M. Heyes, J. Rosen, J. G. Chen, Y. Yan, F. Jiao and B. Xu, *J. Am. Chem. Soc.*, 2017, **139**, 3774–3783.
45 D. Hursán and C. Janáky, *ACS Energy Lett.*, 2018, **3**, 722–723.
46 S. Verma, X. Lu, S. Ma, R. I. Masel and P. J. A. Kenis, *Phys. Chem. Chem. Phys.*, 2016, **18**, 7075–7084.
47 D. Hursán and C. Janáky, *ACS Energy Lett.*, 2018, **3**, 722.
48 O. Ayemoba and A. Cuesta, *ACS Appl. Mater. Interfaces*, 2017, **9**, 27377–27382.
49 F. Zhang and A. C. Co, *Angew. Chem., Int. Ed.*, 2020, **59**, 1674–1681.
50 A. J. Welch, A. Q. Fenwick, A. Böhme, H.-Y. Chen, I. Sullivan, X. Li, J. S. DuChene, C. Xiang and H. A. Atwater, *J. Phys. Chem. C*, 2021, **125**, 20896–20904.
51 Z. Zhang, L. Melo, R. P. Jansonius, F. Habibzadeh, E. R. Grant and C. P. Berlinguette, *ACS Energy Lett.*, 2020, **5**, 3101–3107.
52 D. A. Henckel, M. J. Counihan, H. E. Holmes, X. Chen, U. O. Nwabara, S. Verma, J. Rodríguez-López, P. J. A. Kenis and A. A. Gewirth, *ACS Catal.*, 2021, **11**, 255–263.
53 X. Lu, C. Zhu, Z. Wu, J. Xuan, J. S. Francisco and H. Wang, *J. Am. Chem. Soc.*, 2020, **142**, 15438–15444.
54 A. Roy, D. Hursán, K. Artyushkova, P. Atanassov, C. Janáky and A. Serov, *Appl. Catal., B*, 2018, **232**, 512.
55 B. Endrődi, E. Kecsenovity, A. Samu, F. Darvas, R. V. Jones, V. Török, A. Danyi and C. Janáky, *ACS Energy Lett.*, 2019, **4**, 1770–1777.
56 J. Zhang, W. Luo and A. Züttel, *J. Mater. Chem. A*, 2019, **7**, 26285–26292.
57 A. Ozden, F. Li, F. P. García de Arquer, A. Rosas-Hernández, A. Thevenon, Y. Wang, S.-F. Hung, X. Wang, B. Chen, J. Li, J. Wicks, M. Luo, Z. Wang, T. Agapie, J. C. Peters, E. H. Sargent and D. Sinton, *ACS Energy Lett.*, 2020, **5**, 2811–2818.

58 T. Möller, T. Ngo Thanh, X. Wang, W. Ju, Z. Jovanov and P. Strasser, *Energy Environ. Sci.*, 2021, **14**, 5995–6006.
59 S. Garg, C. A. Giron Rodriguez, T. E. Rufford, J. R. Varcoe and B. Seger, *Energy Environ. Sci.*, 2022, **15**, 4440–4469.
60 S. S. Bhargava, F. Proietto, D. Azmoodeh, E. R. Cofell, D. A. Henckel, S. Verma, C. J. Brooks, A. A. Gewirth and P. J. A. Kenis, *ChemElectroChem*, 2020, **7**, 2001–2011.
61 S. Verma, Y. Hamasaki, C. Kim, W. Huang, S. Lu, H.-R. M. Jhong, A. A. Gewirth, T. Fujigaya, N. Nakashima and P. J. A. Kenis, *ACS Energy Lett.*, 2018, **3**, 193–198.
62 K. Yang, R. Kas and W. A. Smith, *J. Am. Chem. Soc.*, 2019, **141**, 15891–15900.
63 M. C. O. Monteiro, A. Mirabal, L. Jacobse, K. Doblhoff-Dier, S. C. Barton and M. T. M. Koper, *JACS Au*, 2021, **1**, 1915–1924.
64 Y. Xu, J. P. Edwards, S. Liu, R. K. Miao, J. E. Huang, C. M. Gabardo, C. P. O'Brien, J. Li, E. H. Sargent and D. Sinton, *ACS Energy Lett.*, 2021, **6**, 809–815.
65 C. Lee, B. Zhao, J. K. Lee, K. F. Fahy, K. Krause and A. Bazylak, *iScience*, 2020, **23**, 101094.
66 C. M. Gunathunge, V. J. Ovalle and M. M. Waegele, *Phys. Chem. Chem. Phys.*, 2017, **19**, 30166–30172.
67 C. W. Machan, M. D. Sampson, S. A. Chabolla, T. Dang and C. P. Kubiak, *Organometallics*, 2014, **33**, 4550–4559.
68 T. Möller, W. Ju, A. Bagger, X. Wang, F. Luo, T. Ngo Thanh, A. S. Varela, J. Rossmeisl and P. Strasser, *Energy Environ. Sci.*, 2019, **12**, 640–647.
69 X. Sheng, W. Ge, H. Jiang and C. Li, *Adv. Mater.*, 2022, **34**, 2201295.
70 Á. Vass, B. Endrődi, G. F. Samu, Á. Balog, A. Kormányos, S. Cherevko and C. Janáky, *ACS Energy Lett.*, 2021, **6**, 3801–3808.
71 D. Salvatore and C. P. Berlinguette, *ACS Energy Lett.*, 2020, **5**, 215–220.
72 Q. Xu, S. Z. Oener, G. Lindquist, H. Jiang, C. Li and S. W. Boettcher, *ACS Energy Lett.*, 2021, **6**, 305–312.
73 D. G. Wheeler, B. A. W. Mowbray, A. Reyes, F. Habibzadeh, J. He and C. P. Berlinguette, *Energy Environ. Sci.*, 2020, **13**, 5126–5134.
74 D. M. Koshy, S. A. Akhade, A. Shugar, K. Abiose, J. Shi, S. Liang, J. S. Oakdale, S. E. Weitzner, J. B. Varley, E. B. Duoss, S. E. Baker, C. Hahn, Z. Bao and T. F. Jaramillo, *J. Am. Chem. Soc.*, 2021, **143**, 14712–14725.
75 C. W. Li and M. W. Kanan, *J. Am. Chem. Soc.*, 2012, **134**, 7231–7234.
76 J. Heyes, M. Dunwell and B. Xu, *J. Phys. Chem. C*, 2016, **120**, 17334–17341.
77 Á. Vass, B. Endrődi and C. Janáky, *Curr. Opin. Electrochem.*, 2021, **25**, 100621.
78 H. W. Shafaque, J. K. Lee, K. Krause, C. Lee, K. F. Fahy, P. Shrestha, M. Balakrishnan and A. Bazylak, *Energy Convers. Manage.*, 2021, **243**, 114302.
79 K. J. P. Schouten, E. Pérez Gallent and M. T. M. Koper, *J. Electroanal. Chem.*, 2014, **716**, 53–57.
80 Y. C. Tan, K. B. Lee, H. Song and J. Oh, *Joule*, 2020, **4**, 1104–1120.
81 B. Hasa, M. Jouny, B. H. Ko, B. Xu and F. Jiao, *Angew. Chem., Int. Ed.*, 2021, **60**, 3277–3282.
82 M. Li, M. N. Idros, Y. Wu, T. Burdyny, S. Garg, X. S. Zhao, G. Wang and T. E. Rufford, *J. Mater. Chem. A*, 2021, **9**, 19369–19409.
83 J. Zhang, W. Luo and A. Züttel, *J. Catal.*, 2020, **385**, 140–145.
84 R. Krause, D. Reinisch, C. Reller, H. Eckert, D. Hartmann, D. Taroata, K. Wiesner-Fleischer, A. Bulan, A. Lueken and G. Schmid, *Chem. Ing. Tech.*, 2020, **92**, 53–61.
85 C. Zhan, F. Dattila, C. Rettenmaier, A. Bergmann, S. Kühl, R. García-Muelas, N. López and B. R. Cuenya, *ACS Catal.*, 2021, **11**, 7694–7701.
86 K. P. Kuhl, E. R. Cave, D. N. Abram and T. F. Jaramillo, *Energy Environ. Sci.*, 2012, **5**, 7050–7059.
87 S. Verma, S. Lu and P. J. A. Kenis, *Nat. Energy*, 2019, **4**, 466–474.
88 K. U. Hansen, L. H. Cherniack and F. Jiao, *ACS Energy Lett.*, 2022, **7**, 4504–4511.
89 M. Ma, E. L. Clark, K. T. Therkildsen, S. Dalsgaard, I. Chorkendorff and B. Seger, *Energy Environ. Sci.*, 2020, **13**, 977–985.
90 D. S. Hussey, D. Spernjak, A. Z. Weber, R. Mukundan, J. Fairweather, E. L. Brosha, J. Davey, J. S. Spendelow, D. L. Jacobson and R. L. Borup, *J. Appl. Phys.*, 2012, **112**, 104906.
91 H. W. Shafaque, C. Lee, K. F. Fahy, J. K. Lee, J. M. LaManna, E. Baltic, D. S. Hussey, D. L. Jacobson and A. Bazylak, *ACS Appl. Mater. Interfaces*, 2020, **12**, 54585–54595.
92 L. Wang, S. A. Nitopi, E. Bertheussen, M. Orazov, C. G. Morales-Guio, X. Liu, D. C. Higgins, K. Chan, J. K. Nørskov, C. Hahn and T. F. Jaramillo, *ACS Catal.*, 2018, **8**, 7445–7454.
93 A. Ozden, Y. Wang, F. Li, M. Luo, J. Sisler, A. Thevenon, A. Rosas-Hernández, T. Burdyny, Y. Lum, H. Yadegari, T. Agapie, J. C. Peters, E. H. Sargent and D. Sinton, *Joule*, 2021, **5**, 706–719.
94 K. Yang, R. Kas, W. A. Smith and T. Burdyny, *ACS Energy Lett.*, 2021, **6**, 33–40.
95 Y. Kong, H. Hu, M. Liu, Y. Hou, V. Kolivoška, S. Vesztergom and P. Broekmann, *J. Catal.*, 2022, **408**, 1–8.
96 A. Xu, N. Govindarajan, G. Kastlunger, S. Vijay and K. Chan, *Acc. Chem. Res.*, 2022, **55**, 495–503.
97 J. Resasco, L. D. Chen, E. Clark, C. Tsai, C. Hahn, T. F. Jaramillo, K. Chan and A. T. Bell, *J. Am. Chem. Soc.*, 2017, **139**, 11277–11287.
98 M. C. O. Monteiro, F. Dattila, B. Hagedoorn, R. García-Muelas, N. López and M. T. M. Koper, *Nat. Catal.*, 2021, **4**, 654–662.
99 A. Murata and Y. Hori, *Bull. Chem. Soc. Jpn.*, 1991, **64**, 123–127.
100 J. Disch, L. Bohn, S. Koch, M. Schulz, Y. Han, A. Tengattini, L. Helfen, M. Breitwieser and S. Vierrath, *Nat. Commun.*, 2022, **13**, 6099.
101 N. Ul Hassan, M. Mandal, G. Huang, H. A. Firouzjaie, P. A. Kohl and W. E. Mustain, *Adv. Energy Mater.*, 2020, **10**, 2001986.
102 J. R. Varcoe, P. Atanassov, D. R. Dekel, A. M. Herring, M. A. Hickner, P. A. Kohl, A. R. Kucernak, W. E. Mustain, K. Nijmeijer, K. Scott, T. Xu and L. Zhuang, *Energy Environ. Sci.*, 2014, **7**, 3135–3191.
103 I. Vincent, E.-C. Lee and H.-M. Kim, *Sci. Rep.*, 2021, **11**, 293.
104 S. Siracusano, S. Trocino, N. Briguglio, V. Baglio and A. S. Aricò, *Materials*, 2018, 11.
105 K. Yang, M. Li, S. Subramanian, M. A. Blommaert, W. A. Smith and T. Burdyny, *ACS Energy Lett.*, 2021, **6**, 4291–4298.
106 J. Gu, S. Liu, W. Ni, W. Ren, S. Haussener and X. Hu, *Nat. Catal.*, 2022, **5**, 268–276.
107 M. C. O. Monteiro, M. F. Philips, K. J. P. Schouten and M. T. M. Koper, *Nat. Commun.*, 2021, **12**, 4943.
108 N. Wang, R. K. Miao, G. Lee, A. Vomiero, D. Sinton, A. H. Ip, H. Liang and E. H. Sargent, *SmartMat*, 2021, **2**, 12–16.
109 E. L. Clark, M. R. Singh, Y. Kwon and A. T. Bell, *Anal. Chem.*, 2015, **87**, 8013–8020.
110 M. Krödel, B. M. Carter, D. Rall, J. Lohaus, M. Wessling and D. J. Miller, *ACS Appl. Mater. Interfaces*, 2020, **12**, 12030–12042.
111 N. Kato, S. Mizuno, M. Shiozawa, N. Nojiri, Y. Kawai, K. Fukumoto, T. Morikawa and Y. Takeda, *Joule*, 2021, **5**, 687–705.
112 J. L. White, J. T. Herb, J. J. Kaczur, P. W. Majsztrik and A. B. Bocarsly, *J. CO2 Util.*, 2014, **7**, 1–5.
113 W. H. Lee, C. Lim, S. Y. Lee, K. H. Chae, C. H. Choi, U. Lee, B. K. Min, Y. J. Hwang and H.-S. Oh, *Nano Energy*, 2021, **84**, 105859.
114 J. Yano and V. K. Yachandra, *Photosynth. Res.*, 2009, **102**, 241.
115 N. J. Firet, T. Burdyny, N. T. Nesbitt, S. Chandrashekar, A. Longo and W. A. Smith, *Catal. Sci. Technol.*, 2020, **10**, 5870–5885.
116 O. Müller, M. Nachtegaal, J. Just, D. Lützenkirchen-Hecht and R. Frahm, *J. Synchrotron Radiat.*, 2016, **23**, 260–266.
117 J. Timoshenko, A. Bergmann, C. Rettenmaier, A. Herzog, R. M. Arán-Ais, H. S. Jeon, F. T. Haase, U. Hejral, P. Grosse, S. Kühl, E. M. Davis, J. Tian, O. Magnussen and B. Roldan Cuenya, *Nat. Catal.*, 2022, **5**, 259–267.
118 H. S. Jeon, J. Timoshenko, C. Rettenmaier, A. Herzog, A. Yoon, S. W. Chee, S. Oener, U. Hejral, F. T. Haase and B. Roldan Cuenya, *J. Am. Chem. Soc.*, 2021, **143**, 7578–7587.
119 M. Rüscher, A. Herzog, J. Timoshenko, H. S. Jeon, W. Frandsen, S. Kühl and B. Roldan Cuenya, *Catal. Sci. Technol.*, 2022, **12**, 3028–3043.
120 S.-F. Hung, F.-Y. Wu, Y.-H. Lu, T.-J. Lee, H.-J. Tsai, P.-H. Chen, Z.-Y. Lin, G.-L. Chen, W.-Y. Huang and W.-J. Zeng, *Catal. Sci. Technol.*, 2022, **12**, 2739–2743.
121 T. Ding, X. Liu, Z. Tao, T. Liu, T. Chen, W. Zhang, X. Shen, D. Liu, S. Wang, B. Pang, D. Wu, L. Cao, L. Wang, T. Liu, Y. Li, H. Sheng, M. Zhu and T. Yao, *J. Am. Chem. Soc.*, 2021, **143**, 11317–11324.
122 W. H. Lee, C. Lim, E. Ban, S. Bae, J. Ko, H.-S. Lee, B. K. Min, K.-Y. Lee, J. S. Yu and H.-S. Oh, *Appl. Catal., B*, 2021, **297**, 120427.
123 X. Y. Zhang, W. J. Li, J. Chen, X. F. Wu, Y. W. Liu, F. Mao, H. Y. Yuan, M. Zhu, S. Dai, H. F. Wang, P. Hu, C. Sun, P. F. Liu and H. G. Yang, *Angew. Chem., Int. Ed.*, 2022, **61**, e202202298.
124 X. Chen, J. Chen, N. M. Alghoraibi, D. A. Henckel, R. Zhang, U. O. Nwabara, K. E. Madsen, P. J. A. Kenis, S. C. Zimmerman and A. A. Gewirth, *Nat. Catal.*, 2021, **4**, 20–27.

125 X. Chen, D. A. Henckel, U. O. Nwabara, Y. Li, A. I. Frenkel, T. T. Fister, P. J. A. Kenis and A. A. Gewirth, *ACS Catal.*, 2020, **10**, 672–682.
126 N. T. Nesbitt and W. A. Smith, *J. Electrochem. Soc.*, 2021, **168**, 44505.
127 G. Zhang, Y. Cui and A. Kucernak, *ACS Catal.*, 2022, **12**, 6180–6190.
128 K. Krause, J. K. Lee, C. Lee, H. W. Shafaque, P. J. Kim, K. F. Fahy, P. Shrestha, J. M. LaManna, E. Baltic, D. L. Jacobson, D. S. Hussey and A. Bazylak, *J. Power Sources*, 2022, **520**, 230879.
129 H. Hoffmann, M. C. Paulisch, M. Gebhard, J. Osiewacz, M. Kutter, A. Hilger, T. Arlt, N. Kardjilov, B. Ellendorff, F. Beckmann, H. Markötter, M. Luik, T. Turek, I. Manke and C. Roth, *J. Electrochem. Soc.*, 2022, **169**, 044508.
130 H.-P. Iglesias van Montfort and T. Burdyny, *ACS Energy Lett.*, 2022, **7**, 2410–2419.
131 A. S. Leach, J. Hack, M. Amboage, S. Diaz-Moreno, H. Huang, P. L. Cullen, M. Wilding, E. Magliocca, T. S. Miller, C. A. Howard, D. J. L. Brett, P. R. Shearing, P. F. McMillan, A. E. Russell and R. Jervis, *J. Phys.: Condens. Matter*, 2021, **33**, 314002.
132 A. Siebel, Y. Gorlin, J. Durst, O. Proux, F. Hasché, M. Tromp and H. A. Gasteiger, *ACS Catal.*, 2016, **6**, 7326–7334.
133 R. J. K. Wiltshire, C. R. King, A. Rose, P. P. Wells, M. P. Hogarth, D. Thompsett and A. E. Russell, *Electrochim. Acta*, 2005, **50**, 5208–5217.
134 A. J. Keeler, G. R. Salazar-Banda and A. E. Russell, *Curr. Opin. Electrochem.*, 2019, **17**, 90–96.
135 A. Botz, J. Clausmeyer, D. Öhl, T. Tarnev, D. Franzen, T. Turek and W. Schuhmann, *Angew. Chem., Int. Ed.*, 2018, **57**, 12285–12289.
136 M. C. O. Monteiro, S. Dieckhöfer, T. Bobrowski, T. Quast, D. Pavesi, M. T. M. Koper and W. Schuhmann, *Chem. Sci.*, 2021, **12**, 15682–15690.
137 S. Dieckhöfer, D. Öhl, J. R. C. Junqueira, T. Quast, T. Turek and W. Schuhmann, *Chem. – Eur. J.*, 2021, **27**, 5906–5912.
138 P. Grosse, D. Gao, F. Scholten, I. Sinev, H. Mistry and B. Roldan Cuenya, *Angew. Chem., Int. Ed.*, 2018, **130**, 6300–6305.
139 I. Khalakhan, M. Vorokhta, P. Kúš, M. Dopita, M. Václavů, R. Fiala, N. Tsud, T. Skála and V. Matolín, *Electrochim. Acta*, 2017, **245**, 760–769.
140 X. Wang, J. F. de Araújo, W. Ju, A. Bagger, H. Schmies, S. Kühl, J. Rossmeisl and P. Strasser, *Nat. Nanotechnol.*, 2019, **14**, 1063–1070.
141 E. L. Clark and A. T. Bell, *J. Am. Chem. Soc.*, 2018, **140**, 7012–7020.
142 C. J. Bondue and M. T. M. Koper, *J. Electroanal. Chem.*, 2020, **875**, 113842.
143 N. Kardjilov, I. Manke, R. Woracek, A. Hilger and J. Banhart, *Mater. Today*, 2018, **21**, 652–672.
144 J. Banhart, A. Borbély, K. Dzieciol, F. Garcia-Moreno, I. Manke, N. Kardjilov, A. R. Kaysser-Pyzalla, M. Strobl and W. Treimer, Dedic. to Profr. Dr H.-P. Degischer Occas. his 65th Birthd., 2010, 101, 1069–1079.
145 T. M. M. Heenan, C. Tan, J. Hack, D. J. L. Brett and P. R. Shearing, *Mater. Today*, 2019, **31**, 69–85.
146 M. Strobl, I. Manke, N. Kardjilov, A. Hilger, M. Dawson and J. Banhart, *J. Phys. D: Appl. Phys.*, 2009, **42**, 243001.
147 P. Boillat, E. H. Lehmann, P. Trtik and M. Cochet, *Curr. Opin. Electrochem.*, 2017, **5**, 3–10.
148 M. C. Paulisch, M. Gebhard, D. Franzen, A. Hilger, M. Osenberg, S. Marathe, C. Rau, B. Ellendorff, T. Turek, C. Roth and I. Manke, *ACS Appl. Energy Mater.*, 2021, **4**, 7497–7503.
149 Y. Wu, J. I. S. Cho, M. Whiteley, L. Rasha, T. P. Neville, R. Ziesche, R. Xu, R. Owen, N. Kulkarni, J. Hack, M. Maier, N. Kardjilov, H. Markötter, I. Manke, F. R. Wang, P. R. Shearing and D. J. L. Brett, *Int. J. Hydrogen Energy*, 2020, **45**, 2195–2205.
150 R. F. Ziesche, J. Hack, L. Rasha, M. Maier, C. Tan, T. M. M. Heenan, H. Markötter, N. Kardjilov, I. Manke, W. Kockelmann, D. J. L. Brett and P. R. Shearing, *Nat. Commun.*, 2022, **13**, 1616.
151 W. Wang, S. Yu, K. Li, L. Ding, Z. Xie, Y. Li, G. Yang, D. A. Cullen, H. Yu, Z. Kang, J. A. Wrubel, Z. Ma, G. Bender, C. B. Capuano, A. Keane and F.-Y. Zhang, *J. Power Sources*, 2021, **516**, 230641.
152 J. Hack, L. Rasha, P. L. Cullen, J. J. Bailey, T. P. Neville, P. R. Shearing, N. P. Brandon and D. J. L. Brett, *Electrochim. Acta*, 2020, **352**, 136464.
153 F. D. Speck and S. Cherevko, *Electrochem. Commun.*, 2020, **115**, 106739.

